Front. Energy 2020, 14(3): 482–509
https://doi.org/10.1007/s11708-020-0693-0

REVIEW ARTICLE

Shiquan SHAN, Chuyang CHEN, Peter G. LOUTZENHISER, Devesh RANJAN, Zhijun ZHOU, Zhuomin M. ZHANG

Spectral emittance measurements of micro/nanostructures in energy conversion: a review

Abstract Micro/nanostructures play a key role in tuning the radiative properties of materials and have been applied to high-temperature energy conversion systems for improved performance. Among the various radiative properties, spectral emittance is of integral importance for the design and analysis of materials that function as radiative absorbers or emitters. This paper presents an overview of the spectral emittance measurement techniques using both the direct and indirect methods. Besides, several micro/nanostructures are also introduced, and a special emphasis is placed on the emissometers developed for characterizing engineered micro/nanostructures in high-temperature applications (e.g., solar energy conversion and thermophotovoltaic devices). In addition, both experimental facilities and measured results for different materials are summarized. Furthermore, future prospects in developing instrumentation and micro/nanostructured surfaces for practical applications are also outlined. This paper provides a comprehensive source of information for the application of micro/nanostructures in high-temperature energy conversion engineering.

Keywords concentrating solar power (CSP), emittance measurements, high temperature, micro/nanostructure, selective absorber, selective emitter, thermophotovoltaics (TPV)

Received Mar. 19, 2020; accepted Jun. 8, 2020; online Aug. 30, 2020

Shiquan SHAN
State Key Laboratory of Clean Energy Utilization, Zhejiang University, Hangzhou 310027, China; George W. Woodruff School of Mechanical Engineering, Georgia Institute of Technology, Atlanta GA 30332, USA

Chuyang CHEN, Peter G. LOUTZENHISER, Devesh RANJAN,

Zhuomin M. ZHANG (✉)
George W. Woodruff School of Mechanical Engineering, Georgia Institute of Technology, Atlanta GA 30332, USA
E-mail: zhuomin.zhang@me.gatech.edu

Zhijun ZHOU (✉)
State Key Laboratory of Clean Energy Utilization, Zhejiang University, Hangzhou 310027, China
E-mail: zhouzj@zju.edu.cn

1 Introduction

In recent years, renewed interest in power generation using solar energy has attracted widespread attention as a means to expedite the transition away from fossil fuels while increasing electricity production and mitigating anthropogenic CO_2 emissions. Of special interest are two solar technologies for producing electricity as schematically depicted in Fig. 1: the concentrating solar power (CSP) system [1,2], and the thermophotovoltaics (TPV) system [3–5].

CSP is a relatively mature technology for solar energy thermal utilization. Figure 1(a) shows a schematic of a typical solar power tower CSP system consisting of three subsystems: a heliostat field, a molten salt thermal energy storage system, and a thermal power cycle. Direct solar irradiation impinges upon the heliostat mirrors during operation that is redirected to a solar receiver mounted on top of the solar tower. Molten salt is used as a thermal energy storage medium and is circulated from a cold storage unit into the solar receiver where it is heated by the concentrated solar irradiation, and then moved to a hot storage tank. An integrated heat exchanger is used to transfer the heat from the molten salt to the working fluid to provide heat to the power cycle when required. Work is produced from the turbine and used to produce on-demand electricity. Operating at elevated temperatures is integral for improving the efficiency of the CSP thermal power cycle; thus, the supercritical CO_2 Brayton cycle operating at a high temperature from 500°C to 800°C has been extensively studied [2,6]. Operating at higher cycle temperatures requires increasing the solar receiver temperature, which results in an increase in the thermal emission to the surroundings and a subsequent reduction of the collection efficiency [7]. Therefore, a selective

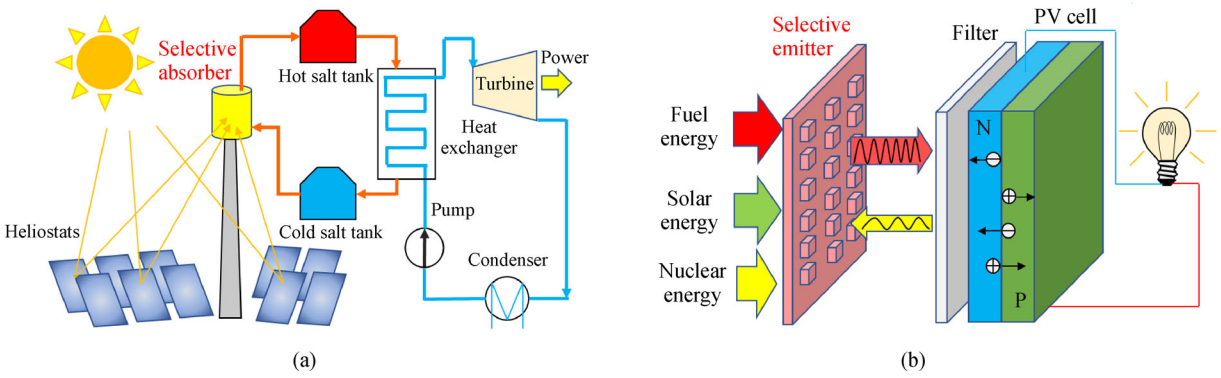

Fig. 1 Schematic diagram.
(a) CSP system; (b) TPV system.

absorber that has a higher absorptance for solar irradiation and a lower infrared emittance at a high temperature is critical for CSP application to harvest solar energy more efficiently [8,9].

TPV is another attractive technology that converts thermal radiation to electricity. As shown in Fig. 1(b), a TPV system consists of a heat source with a selective emitter, an optional filter, and a photovoltaic (PV) cell. Contrary to the traditional thermal power cycles, TPV devices convert the photon energy directly to electricity without any moving parts. Heat can be produced from fuel or waste combustion, solar radiation, or nuclear reaction to increase the emitter temperature, so that photon energies above the bandgap of a PV cell can be utilized to generate photocurrent [10]. Since the bandgap of typical PV cells used in TPV systems is in the near infrared, only a small portion of photons whose energy is greater than the bandgap energy can produce electron-hole pairs in a PV cell. The sub-bandgap photons at longer wavelengths cannot generate photocurrent and thus are lost to heat. To improve the TPV conversion efficiency, selective emitters have been proposed and developed to match the spectral quantum efficiency of PV cells [4,9]. Depending on the particular PV cell used, a selective emitter should have a high emittance at shorter wavelengths and a low emittance at longer wavelengths, although in some cases, a narrowband emitter is of interest. In addition, placing a filter as shown in Fig. 1(b) is another option. However, this design requires additional selectivity materials and is more complicated. Concentrated solar irradiation may be used as the heat source and the combined system is termed as a solar TPV system [11,12]. Solar TPV has an integrate absorber on the front side for solar energy harvesting and an emitter on the back side for thermal radiative emission. Both a selective solar absorber and a selective emitter are required to improve the system efficiency [13,14].

Recently, micro/nanostructures have attracted a lot of attention because they enable the tuning of spectral and directional thermal radiative properties [9,10,15], especially for the design of selective absorbers/emitters in CSP and TPV applications. Because both CSP and TPV systems theoretically perform better at higher temperatures, engineered micro/nanostructures capable of withstanding high temperatures have recently been examined as candidates of selective absorbers/emitters. Typical structures include multilayers, periodic gratings, metamaterials, as well as photonic crystals [15,16]. This area of research benefits from technological innovations in micro- and nano-patterning on surfaces. To fine tune their properties to effectively emit radiation in the desired wavelength region or absorb solar irradiation, special structures have been designed to enhance or suppress the absorption/emission at different wavelengths. In addition, tuning the radiative properties with angular and polarization responses, as well as real-time tuning, has also been explored and realized [16]. With the employment of micro/nanostructures, the efficiency of energy conversion in TPV systems could be dramatically improved via reduction of the sub-bandgap losses in PV cells [17]; the improvement in CSP systems could be realized via reduction of the loss in the solar absorber [8]. Therefore, investigation on the thermal emittance characteristics of micro/nanostructures can guide the research and design of CSP and TPV systems in terms of the structural design and material selection.

The study of emittance for micro/nanostructures encompasses both numerical calculations and experimental measurements [18]. Generally, both emittance measurements [19] and calculations [20] include the direct method and the indirect method. The latter uses the reflectance to calculated emittance based on Kirchhoff's law. Measurements of the spectral emittance of micro/nanostructures are critically important to validate the numerical predictions, especially at high temperatures. Honner and Honnerova [19] reviewed the conventional emittance measurement techniques, while Jones et al. [21] provided a survey of the emittance measurements for materials at high temperatures. Many laboratories have developed their own measurement setups [22–29] mainly for measuring the emittance of metals and their oxides. Although the general measurement techniques are applicable to micro/nanos-

tructures, directionality and polarization dependence are much more meaningful in the study of micro/nanostructured materials and surfaces [25]. There exist some reviews on the radiative properties of micro/nanostructures with a focus on simulation and measurement results [18,30,31] or applications in energy conversion [17,32]. Due to the rapid development in this field, an updated literature survey covering both the instrumentation and the measurement results, especially techniques for measuring emittance of micro/nanostructures at high-temperature application, is much needed.

The present paper is intended to address the lack of a comprehensive summary in the literature of high-temperature emissometry for micro/nanostructured surfaces. The two main objectives are to provide a survey of the research on spectral emittance measurements for micro/nanostructured materials and to provide a reference for the application on high-temperature engineering such as solar energy conversion and TPV. Typical and unique emissiometry techniques are discussed and the results of emittance measurement for micro/nanostructures are reviewed. The definition of emittance is introduced and the commonly used measurement techniques are summarized. A review of typical and unique measurement apparatuses and major facilities is provided. The basics of different micro/nanostructures are introduced and the measured emittance spectra as selective TPV emitters and selective solar absorbers in high-temperature energy conversion are reviewed. Finally, an overall summary of the work and outlook for the future development in this field are provided.

2 Emittance definition and measurement methods

This section begins with the fundamentals of thermal radiation and the definition of various terms associated with the emittance of materials [16,33–35]. Afterward, measurement principles for the direct method and indirect method are introduced.

2.1 Background of blackbody radiation and the emittance definition

The spectral emissive power of a real object (or surface) is always smaller than that of a blackbody at the same temperature into the same medium at any given direction. The ratio of the radiant power emitted by a real surface per unit area to that of a blackbody at the same temperature is called the emittance. Due to its dependence on wavelength and direction, and even polarization, it is important to specify whether the emittance is spectral or total, directional or hemispherical, single polarization or polarization-averaged, etc. Generally speaking, "emittance" is used to refer to the property of a specific object that depends on the thickness, surface roughness, oxidation, etc. "Emissivity" is often used interchangeably with "emittance" in the literature. Nevertheless, there is a subtle distinction between them as some authors have suggested using "emissivity" as an intrinsic property of an opaque material with an optically smooth surface [16,33,36]. In this paper, "emittance" is used uniformly for all materials regardless of what the original publications use. An attempt is made to distinguish different emittance definitions with adjectives such as spectral, directional, hemispherical, total, etc. However, in most cases, the specifics can be found from the context without spelling out all the details.

The spectral emissive power in the vacuum of a blackbody ($E_{b,\lambda}(\lambda, T)$) at absolute temperature T is described by Planck's law as

$$E_{b,\lambda}(\lambda,T)=\frac{C_1\lambda^{-5}}{e^{C_2/(\lambda T)}-1}, \tag{1}$$

where λ in [μm] is the wavelength in vacuum, $C_1 = 3.742\times10^8$ W·μm^4·m^{-2} and $C_2 = 1.439\times10^4$ μm·K are the first and second radiation constant, respectively. The total emissive power of a blackbody ($E_b(T)$) is determined by integrating Eq. (1) over all wavelengths,

$$E_b(T)=\int_0^\infty E_{b,\lambda}(\lambda,T)\mathrm{d}\lambda=\sigma T^4, \tag{2}$$

which is the Stefan-Boltzmann law, and $\sigma = 5.670\times10^{-8}$ W·m^{-2}·K^{-4} is called the Stefan-Boltzmann constant. The radiant power emitted per unit area, per unit solid angle, and per unit wavelength interval defines the spectral intensity I_λ, and its integration over all wavelengths gives the total intensity I_{total} or simply I. The emissive power of a surface of an object ($E_\lambda(\lambda, T)$) can be expressed in terms of the intensity integrated over the hemisphere considering the projected area and solid angle as

$$E_\lambda(\lambda,T)=\int_0^{2\pi}\int_0^{\pi/2} I_\lambda(\lambda,T,\theta,\psi)\cos\theta\sin\theta\mathrm{d}\theta\mathrm{d}\psi. \tag{3}$$

For a diffuse surface, since the intensity is not a function of the zenith angle θ and azimuthal angle ψ, Eq. (3) yields $E_\lambda = \pi I_\lambda$ and furthermore, $E = \pi I$ also holds for a diffuse surface. By definition, a blackbody is a diffuse surface; therefore, $I_{b,\lambda}(\lambda, T) = E_{b,\lambda}(\lambda, T)/\pi$ and $I_b(T) = \sigma T^4/\pi$.

Next, the expressions of emittance are given according to the definitions of emissive power and radiation intensity. The spectral, directional emittance $\varepsilon_{\lambda,\theta}(\lambda, T, \theta, \psi)$ is defined as

$$\varepsilon_{\lambda,\theta}(\lambda,T,\theta,\psi)=\frac{I_\lambda(\lambda,T,\theta,\psi)}{I_{b,\lambda}(\lambda,T)}. \tag{4}$$

The spectral, hemispherical emittance $\varepsilon_\lambda(\lambda, T)$ is defined based on the emissive power,

$$\varepsilon_\lambda(\lambda,T)=\frac{E_\lambda(\lambda,T)}{E_{\mathrm{b},\lambda}(\lambda,T)},$$

which can be expressed in terms of the spectral emissive power using Eqs. (3) and (4), i.e.,

$$\varepsilon_\lambda(\lambda,T)=\frac{1}{\pi}\int_0^{2\pi}\int_0^{\pi/2}\varepsilon_{\lambda,\theta}(\lambda,T,\theta,\psi)\cos\theta\sin\theta\mathrm{d}\theta\mathrm{d}\psi. \quad (5)$$

Moreover, the total, hemispherical emittance $\varepsilon(T)$ is defined based on the total emissive power and can be expressed as a weighted integral of the total, spectral emittance as

$$\varepsilon(T)=\frac{E(T)}{E_\mathrm{b}(T)}=\frac{1}{\sigma T^4}\int_0^\infty\varepsilon_\lambda(\lambda,T)E_{\mathrm{b},\lambda}(\lambda,T)\mathrm{d}\lambda. \quad (6)$$

In practice, the emittance is often determined from the absorptance by applying Kirchhoff's law, which was originally derived under thermodynamic equilibrium based on the energy balance [16]. In general, the absorptance and emittance of a given material are not the same. For most materials, however, the spectral directional radiative properties are intrinsic properties that do not depend on the surrounding irradiation environment. Therefore, the spectral directional absorptance $\alpha_{\lambda,\theta}(\lambda, T, \theta, \psi)$ equals the spectral directional emittance $\varepsilon_{\lambda,\theta}(\lambda, T, \theta, \psi)$ without requiring thermal equilibrium [35], i.e.,

$$\alpha_{\lambda,\theta}(\lambda,T,\theta,\psi)=\varepsilon_{\lambda,\theta}(\lambda,T,\theta,\psi). \quad (7)$$

For an opaque surface according to the energy balance, the sum of the absorptance and reflectance equals unity, so that the emittance can be deduced indirectly from reflectance measurements. Furthermore, for a diffuse-gray surface, Kirchhoff's law can be applied to the total, hemispherical absorptance and emittance without requiring thermal equilibrium. While Eq. (7) can be applied to any individual polarization for nanostructured materials and metamaterials, special cases occur when Kirchhoff's law may break down, such as nonlinear materials and magneto-optical materials. In all the discussed micro/nanostructures for high-temperature applications reviewed in this paper, Kirchhoff's law is assumed to hold for spectral, directional properties.

2.2 Measurement principles

The emittance measurement methods include the calorimetric method and direct and indirect methods [33]. The calorimetric method based on the net radiative heat loss or gain of an isolated specimen is only suitable for measuring the total hemispherical emittance of a surface [37,38]. The calorimetric method was mainly used several decades ago for measuring the total emittance of metals and refractory materials at very high temperatures. Since this review is mainly focused on the spectral radiative properties, the calorimetric method will not be further discussed. The direct and indirect methods are widely used [22–29,39–50] and the measurement principles are outlined here.

2.2.1 Direct method

The direct method is based on the definition of emittance, i.e., the ratio of the emitted radiative power from the specimen to that from a blackbody at the same temperature with the same geometric arrangement. A spectrophotometer is typically used to measure the spectral emittance. The emission in normal or near-normal directions is frequently taken in the measurements without a polarizer. The spectral emittance of the sample in a given direction is obtained from Eq. (4) and rewritten as

$$\varepsilon_\lambda(\lambda,T)=\frac{L_{\mathrm{s},\lambda}(\lambda,T)}{L_{\mathrm{b},\lambda}(\lambda,T)}, \quad (8)$$

where $L_{\mathrm{s},\lambda}(\lambda, T)$ and $L_{\mathrm{b},\lambda}(\lambda, T)$ represent the measured spectral intensity or radiance from the sample and from the blackbody, respectively [34]. In spectrometric measurements, the absolute value of the intensity is not required. Typically, only the sample and blackbody spectra are measured by assuming that the detector responds to the radiative flux linearly. However, it is necessary to consider the background radiation entering the detector. Hence, the practical measurement equation for the spectral emittance can be expressed as

$$\varepsilon_\lambda(\lambda,T)=\frac{V_{\mathrm{s},\lambda}(\lambda,T)-V_{0,\lambda}(\lambda)}{V_{\mathrm{b},\lambda}(\lambda,T)-V_{0,\lambda}(\lambda)}, \quad (9)$$

where $V_{\mathrm{s},\lambda}$ and $V_{\mathrm{b},\lambda}$ are the output spectra for the sample and blackbody, respectively, and $V_{0,\lambda}$ denotes the contribution to the spectrum by background radiation, which could be measured using a blackbody at a much lower temperature, such as the liquid-nitrogen temperature [22,23]. Another way to determine the background radiation spectrum is to use the blackbody spectra at two different temperatures [27]. The measured blackbody spectra at different temperatures also enable the determination of the instrument response function. Together with the sample spectrum, the sample emittance can be determined [45]. Nevertheless, when the sample temperature is sufficiently high, background radiation is neglected. There are various sources of uncertainties due to the equivalence of the optical paths between the sample and blackbody, sample reflectance effect, uncertainty in the sample temperature measurements, nonlinearity of the detector, and errors in the spectrophotometer [45–47]. Thus, various techniques and modifications have been applied to improve the measurement accuracies [23–27]. Further review of specific instrumentation and facility using the direct method will be given in Section 3.1.

2.2.2 Indirect method

The indirect method for measuring the emittance is based on Kirchhoff's law, typically for opaque materials. As given in Eq. (7), the spectral, directional emittance is equal to the spectral, directional absorptance. Based on the energy balance, the sum of spectral, directional absorptance and the spectral, directional-hemispherical reflectance from an opaque surface equals unity [33–35]. Therefore, the spectral, directional emittance is indirectly determined from the spectral, directional-hemispherical reflectance $\rho_{\lambda,\theta}(\lambda, T, \theta, \psi)$ as

$$\alpha_{\lambda,\theta}(\lambda,T,\theta,\psi) = 1-\rho_{\lambda,\theta}(\lambda,T,\theta,\psi). \quad (10)$$

For specular surfaces, the directional-hemispherical reflectance is the same as the specular reflectance. Thus, the specular reflectance spectra can be measured by a grating monochromator or a Fourier-transform infrared (FTIR) spectrometer using suitable reflectance accessories [16,40]. For non-specular surfaces such as those with surface roughness or micro/nanostructures, an integrating sphere is commonly used to measure the directional-hemispherical reflectance [41,42].

The spectral directional emittance can be integrated over the hemisphere using Eq. (5) to obtain the spectral hemispherical emittance. Furthermore, integration over all wavelengths yields the total emittance. Notice that the total emittance is a function of the sample temperature according to Eq. (6). Most indirect measurements have been performed for samples near room temperature only. To apply Eq. (6) to calculate the total emittance at high temperatures, the assumption must be made that the spectral emittance or absorptance is independent of temperature. Nevertheless, there are some instruments for high-temperature measurements [28,29] that can be used to measure the emittance indirectly for CSP or TPV applications. The setup and operation principles of these instruments will be discussed in Section 3.2.

3 Instrumentation for emittance measurements

This section reviews typical instruments and standard facilities used for measuring emittance, using both the direct (Section 3.1) and indirect (Section 3.2) methods. Note that most of the micro/nanostructures are fabricated on metal or dielectric substrates. The lateral extension of these materials is usually large enough to be considered as macroscale (several centimeters or larger) for practical applications. Therefore, most of the traditional spectrometric measurement instruments can be directly applied to characterize the absorptance and emittance of micro/nanostructured materials [16,34]. In some cases, the directional selectivity and polarization dependence need to be considered; subsequently, specially designed instruments are necessary. In other cases, it is desired to use an infrared microscope to study the local emittance with tens of micrometers resolution. Nevertheless, this review does not consider instruments with subwavelength resolution based on near-field microscopy [16].

3.1 Direct measurements

Many laboratories throughout the world have used the direct measurement apparatuses as the main emittance measurement method with added modifications under different measurement conditions. A representative experimental setup [27] for measuring the spectral directional emittance is schematically shown in Fig. 2 and used here to explain the basic components and methodology. This emissometer is composed of four modules: a blackbody, a sample chamber, an FTIR spectrometer, and an optical entrance box with a mirror/window assembly. Measurement instruments and facilities have been developed elsewhere with similar or somewhat modified configurations [39,43,44]. Commercial blackbody furnaces are often used as a reference source. Parabolic and/or ellipsoidal mirrors are used to focus or collimated light at desired optical path locations. As shown in Fig. 2, the blackbody is separated from the optical entrance box by an infrared window (e.g., KBr). The switching between the blackbody and the sample can be performed by rotating a flip mirror. This arrangement achieves an identical optical path from the blackbody or the sample to the detector. A heated sample holder is placed inside the chamber and can be rotated by a stepper motor to vary the angle of emission (θ). The sample is electrically heated by a resistive spiral wire and the sample temperature is measured by a K-type thermocouple in contact with the resistive wire. The sample temperature is controlled by a proportional-integral-derivative (PID) device. The temperature uniformity of better than ± 2 K can be achieved at temperatures up to 1050 K. The measurement spectral region is from 1.3 μm to 25 μm, as determined by the FTIR system. The spectrometer, sample chamber, and blackbody are sealed and evacuated to eliminate absorptions due to the water vapor and carbon dioxide in the ambient. Some systems (to be discussed later) use dry air or nitrogen gas to purge the optical path to reduce the H_2O and CO_2 gas absorption. The emittance uncertainties result from the signal-to-noise ratio of the measured spectral signals as well as uncertainties in the temperature measurements, among others. The overall measurement uncertainty can be estimated by the root-mean-square of the values of all uncertainty components. In many practical high-temperature emissometry setups, the main contribution to the uncertainty is from the sample temperature measurement. The overall uncertainty for the setup shown in Fig. 2 at intermediate temperatures is less than 3% [27]. Detailed discussions on the uncertainty analysis of spectral emissiometry can also be found in Refs. [45,46].

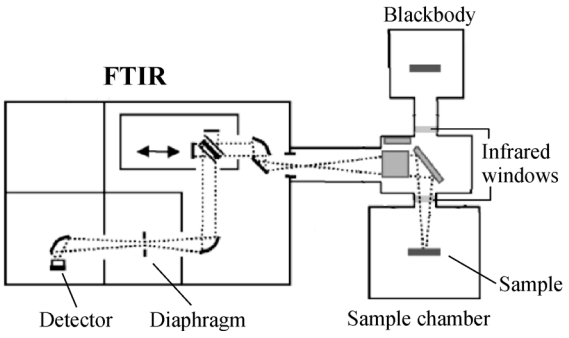

Fig. 2 Schematic diagram of a high-temperature spectral emissometer (reprinted from Ref. [27] with permission).

Physikalisch-Technische Bundesanstalt (PTB) is the National Metrology Institute of Germany and has done pioneering measurements of blackbody emission spectrum, leading to the discovery of Planck's law [34]. Two setups for direct emittance measurements at PTB are outlined here: the emittance measurement in air facility (EMAF) as demonstrated in Fig. 3(a) [22,47], and the reduced background calibration facility (RBCF) for measurements under vacuum as displayed in Fig. 3(b) [23,48]. The operating principles of both setups are similar and rooted in direct measurement techniques. The EMAF measures the spectral, directional emittance of materials in air with an FTIR spectrometer of 4–40 μm. The sample holder can also be rotated for directional measurements,

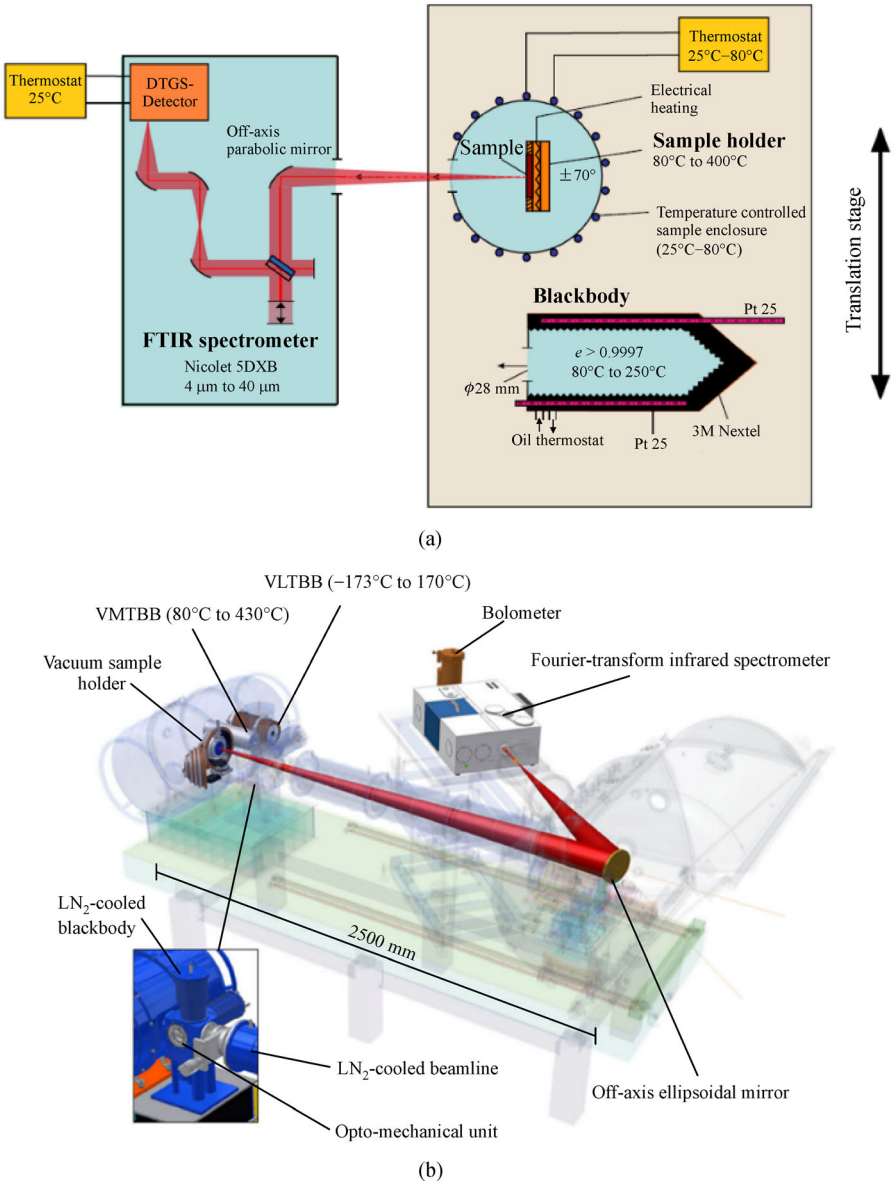

Fig. 3 Experimental setup of PTB for measuring the spectral directional emittance.
(a) In air condition [47]; (b) in vacuum condition [48] (reprinted from Refs. [47,48] with permission).

and the sample temperature is controlled via heating with an electrical resistor. A translational stage can be used to select irradiation from either the sample or the blackbody for measuring the sample spectrum and blackbody spectrum, respectively. The estimated uncertainty of EMAF is 0.01 for samples with an emittance above 0.6 at temperatures from 200°C to 400°C [47]. The RBCF facility illustrated in Fig. 3(b) has two vacuum blackbodies for temperature ranges nominally from −173°C to 170°C and from 80°C to 430°C, respectively. All the components and optical paths are under vacuum conditions and the sample emittance can be measured for $0° \leqslant \theta \leqslant 70°$ in the wavelength range from 1 μm to 1000 μm. The RBCF uses a bifilarly wound resistive wire to heat the sample. The reported uncertainty in the measured spectral emittance is less than 0.01 at wavelengths from 4 μm to 100 μm in the temperature range from about –40°C to 450°C [48]. The spectral hemispherical emittance at the measured temperature and the total hemispherical emittance can be obtained by integrating the spectral directional emittances, according to Eqs. (5) and (6), respectively.

Researchers at the National Institute of Standards and Technology (NIST) in USA have constructed an infrared spectral emittance measurement facility as exhibited in Fig. 4 [24,49]. Three variable temperature blackbodies are used: a water blackbody as a stable room-temperature source, a cesium (Cs) heat-pipe blackbody for the temperature range of 300°C–650°C, and a sodium (Na) heat-pipe blackbody for the temperature range of 550°C–1100°C. The heat pipes are temperature controlled with a center-mount Pt resistance thermometer. All blackbody references can be purged by dry air. A fourth blackbody (not shown in Fig. 4) that is cooled by liquid nitrogen (78 K) can be used for background measurement to obtain $V_{0,\lambda}$ in Eq. (9) [49]. The corresponding Cs and Na heat pipes are also used to heat the sample to match the blackbody temperature ranges. A key feature of this facility is that the sample is mounted behind an integrating sphere for high-temperature reflectance measurements. This enables a noncontact measurement of the sample surface temperature for comparison to the thermocouple meassurement. The reflectance measured at selected wavelengths can be used to calculate the emittance indirectly according to Eq. (10). The details of the indirect measurement will be deferred to Section 3.2. The integrating sphere can be removed for measuring the sample radiance using the FTIR spectrometer (or a filter radiometer) and compared to that from a blackbody at the corresponding temperature to obtain the infrared emittance from about 1 μm to 20 μm with varying emission angles. The reported overall uncertainty (95% confidence level) is 2.9% for a Pt-10Rh sample (whose emittance varies from 0.03 to 0.18) and 0.93% for a SiC sample (whose emittance varies from 0.05 to 0.99) [24].

Wang et al. [25,50] developed a high-temperature emissometer for measuring polarization-dependent emittance of micro/nanostructured materials, as presented in Fig. 5. The unique feature of this design lies in the use of an ellipsoidal mirror to collect the radiation from either the blackbody or the sample (with the flip mirror). With a relatively long focal length from the sample to the ellipsoidal mirror of around 500 mm, the collection angle from the sample is confined to a half-cone angle of 3°. A computer-controlled rotary stage allows varying the emission angle from 0° to 60° with a resolution of 0.01°, providing a high angular resolution for measuring the

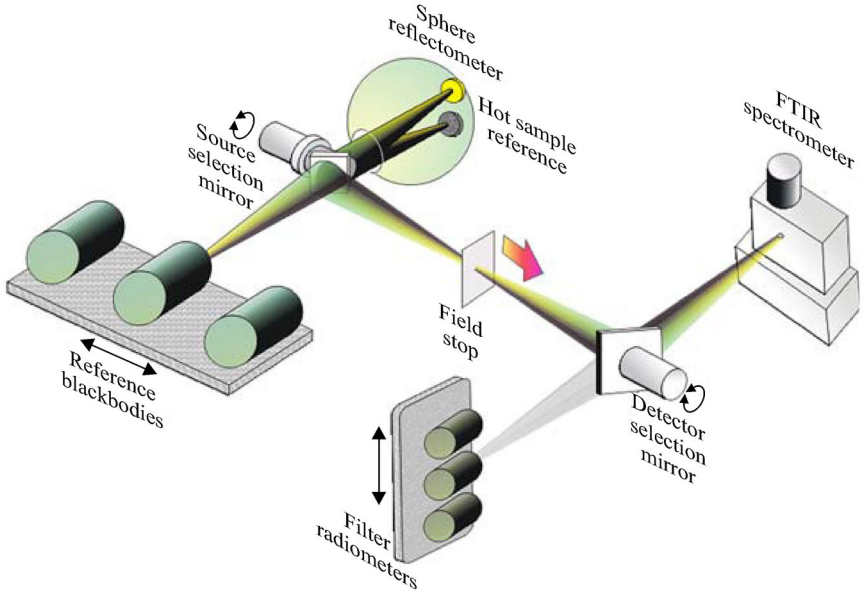

Fig. 4 Schematic of the infrared spectral emittance characterization facility at NIST (reprinted from Ref. [24] with permission).

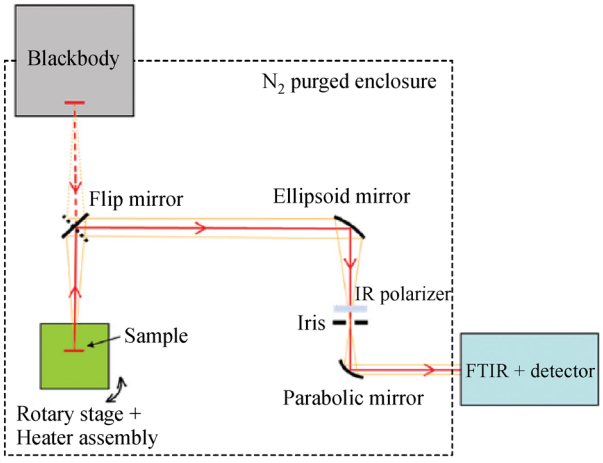

Fig. 5 Optical layout of the high-temperature spectral emissometer at the Georgia Institute of Technology (reprinted from Ref. [25] with permission).

directional emittance of the micro/nanostructure. An iris (aperture) is placed in the common focal point between the ellipsoidal mirror and the parabolic mirror to adjust the collection area on the sample and the radiation entering the FTIR. Before the iris, an IR polarizer is used to select the polarization and then the parabolic mirror sends collimated beam to the FTIR. A pyroelectric (DTGS) detector is used for sample temperatures higher than 700 K at wavelengths from about 2.0 μm to 20 μm, while a liquid-nitrogen-cooled indium antimonite (InSb) detector is used at temperatures above 500 K at wavelengths from 2.0 μm to 5.5 μm. The sample is heated up to 1000 K by an electrical coil heater. A K-type thermocouple probe with oxidation-resistive sheathing is embedded inside the copper disk for sample temperature measurement, and a PID temperature controller allows the sample temperature to be maintained at the set point. Measurements of the fabricated multilayered and microstructured samples have been made and will be discussed in Section 4.3.2 [25,50].

An emissiometry facility at the National Institute of Optics in Italy is equipped with directional view ports, as shown in Fig. 6, and uses a rotating parabolic mirror to direct the emission either from the sample or the blackbody to the FTIR spectrometer [26]. The vacuum chamber with a furnace that is used to heat the sample has three viewports: the main viewport with a ZnSe window is used to measure the radiation emitted by the sample at $\theta = 0°$ (normal direction); while the other two viewports are used to measure the emission at $\theta = 45°$ and 70°, respectively. A recirculating cooling water system is used to maintain furnace walls at near-room temperature. To ensure the same optical path length, the sample and blackbody aperture are located at the same distance with respect to the center of the rotating mirror. The sample is placed on the cylindrical electrical heater and locked with three clips. Three S-type thermocouples are used to measure the surface temperature of the sample at different locations, and a K-type thermocouple is used to measure and help control the heater temperature. This facility can measure sample temperatures from 500 K to 1100 K at wavelengths of 2.5–20 μm in high vacuum and has been used for measuring high-temperature solar absorbing materials such as hafnium carbide (HfC) and tantalum diboride (TaB_2). The estimated uncertainty of measured emittance is 10%, largely due to the sample temperature measurement uncertainty, which is 5% at temperatures above 1000 K [26].

A number of direct measurement setups have been developed with different layouts and objectives besides the applications of CSP and TPV. Different detecting systems can also be utilized for direct measurement rather than FTIR spectrometer, such as the thermal detector [39] and photon detector [51] coupled with a grating monochromator or spectroradiometer [52]. Ma et al. [53] developed a

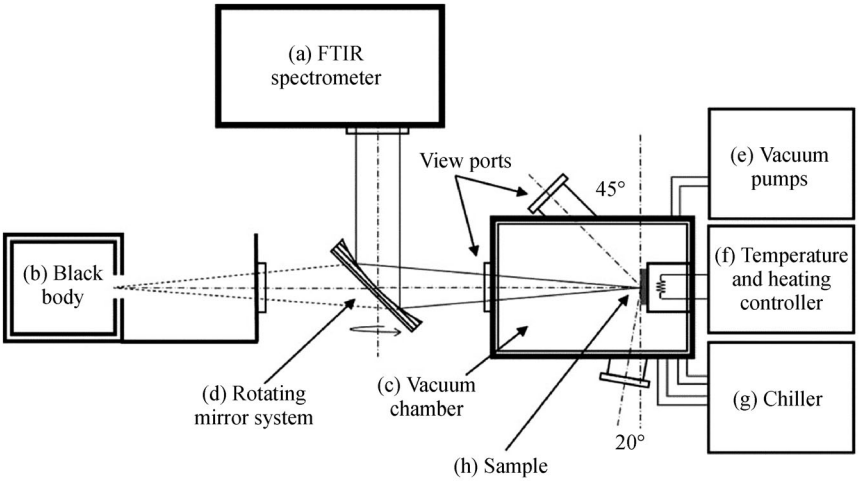

Fig. 6 The vacuum emissiometry setup at the National Institute of Optics in Italy (reprinted from Ref. [26] with permission).

setup with a refrigerator for measuring the emittance of spacecraft materials from 173 K to 213 K. Honnerová et al. [54] and Honner et al. [55] developed a laser scanning heating method for high-temperature emittance measurements. Measurement systems have also been developed using a solar simulator as the heater for measuring the emittance of a cobalt chromium-nickel alloy and pure niobium at high temperatures for the Solar Orbiter mission [52] or the emittance of lunar soils [56]. In another study, Cao et al. [57] constructed an instrument for gas-cooled, high-temperature reactor materials using a rotating sample holder with seven sample holes and one blackbody hole to achieve fast switching between the reference and sample measurements. Gorewoda and Scherer [58,59] devised a measurement setup to study the emittance of carbonates and sulfates in coal ashes from oxyfuel combustion.

Several measurement systems have been developed for studying micro/nanostructures. Hesketh et al. [60,61] used a spectral emissometer to demonstrate the effect of cavity resonance mode on the emittance of microgrooved silicon surfaces. Kusunoki et al. [62] built a system for measuring microstructures with a rotating stage and FTIR spectrometer. Sai et al. [63] devised an apparatus for measuring the emittance of surface-relief gratings as TPV emitters and used an oxygen-gas torch burner to heat the sample [64]. Kirikae et al. [65] constructed a setup consisting of a vacuum chamber, an infrared heat lamp, an IR spectrometer, and a sample holder made of amorphous graphite. Hanamura and Kameya [66] developed an emissiometry setup using CO_2 laser to heat the microstructured sample to near 1000 K.

Table 1 summarizes some representative experimental systems from the literature for directional, spectral emittance measurements. The key features are listed, including the detecting instrument, wavelength range, sample temperature range, directionality, heating method, and facility location. Electric heating is widely used for medium-to-high temperatures from 100°C to above 1000°C, while torch heating [44,64,67] and solar furnace [52,56] can be used for higher temperatures from 1500°C to 2000°C. When the temperature is less than 100°C, circulating fluid [68] can be used in the range from 0°C to 100°C, and refrigeration equipment is required for temperatures below 0°C [53]. FTIR spectrometer is mostly used as the primary detection system from the near-infrared to the far-infrared regions. Most systems measure the normal emittance with fewer systems capable of measuring directional emittance. However, measuring directional emittance is much more important for micro/nanostructures due to their directional optical characteristics. Nearly all of the samples are measured under vacuum or in an inert environment to avoid the influence of CO_2 and H_2O absorption in the air, with the exception of Ref. [39], where an atmospheric environment was used to investigate the effects of oxidation. The direct method is more suitable for medium and high-temperature measurement; however, measuring the emission intensity below 3 μm at near-room temperature cannot be easily performed due to the very low spectral emissive power.

3.2 Indirect measurements

For indirect measurements when samples are at room temperature, a grating monochromator or FTIR spectrometer can measure the specular reflectance or diffuse reflectance with suitable accessories [40–42]. Typically, specular reflectance accessories consist a set of mirrors, and diffuse reflectance can be measured with an integrating sphere. The inner wall of the sphere is made of a high diffuse reflector, such as PTFE for the ultraviolet (UV), visible (VIS), and near-infrared (NIR) regions or a gold-coated diffuse reflector for the NIR and mid-infrared (MIR) regions. Oftentimes, when the properties at elevated temperatures are not available, the assumption that the spectral emittance (or reflectance) is not a function of temperature has been made and the weighted integration of Eq. (6) can be applied to obtain the total emittance at specified temperatures. These instruments will not be reviewed here. Some specially designed instruments measure the reflectance of samples at high temperatures and then deduce the emittance as discussed in the subsequent paragraphs.

Figure 7 shows the detailed layout of the NIST facility with the indirect measurement scheme [28]. It is the same facility as shown in Fig. 4 with the FTIR spectrometer omitted, with additional details on the integrating sphere, and with the light source on the right of the sphere. The main purpose is to provide accurate radiometric temperature measurement of the front surface of the sample while, in the meantime, obtaining the near normal ($\theta = 8°$) emittance at a specific NIR wavelength using one of the filter radiometers. The actual layout of all modules is not in a plane but rather collapsed. The tungsten halogen lamp light is guided to the integrating sphere from the rear port using a bundle of optical fibers that illuminates the wall of the integrating sphere, except the sample or reference using baffles to block the incident light. The sample is irradiated hemispherically since the integrating sphere reflects the light multiple times to produce a nearly uniform hemispherical incidence on the sample surface. The component that exits the front port of the sphere is reflected and passes through a filter wheel to a Si or InGaAs photodiode, as shown in Fig. 7. Narrowband optical filters at the wavelengths of 0.905 μm and 1.55 μm are matched with the corresponding photodiode in the filter radiometer module. Since the illumination is modulated with a mechanical chopper, a lock-in amplifier is used to measure the output signal due to reflection, irrespective of the sample temperature. For the integrating sphere measurement, a reflector needs to be used as the reference that is mounted interchangeably with the sample. This setup measures the hemispherical-directional reflectance of

Table 1 Summary of direct emittance measurement instruments

Detecting instrument	Wavelength /μm	Temperature /K	Directionality	Heating method	Organization	References
FTIR	4–40	353 to 673	Directional (5° to 70°) and hemispherical	Electrical heater	PTB (No. 1, Germany)	[22,47]
FTIR	1–1000	273 to 703	Directional (0° to 70°) and hemispherical	Bifilarly wound wire heater	PTB (No. 2, Germany)	[23,48]
FTIR	1–20	600 to 1400	Directional (0° to 75°)	Cs and Na heat-pipe heater	NIST (USA)	[24,49]
FTIR	2–19	Up to 1000	Directional (0° to 60°)	Electrical coil heater	Georgia Institute of Technology (USA)	[25,50]
FTIR	2.5–20	500 to 1200	Normal, 45° and 70°, and hemispherical	Electric heating	CNR-INO National Institute of Optics (Italy)	[26]
FTIR	1.3–25	Ambient to 1050	Directional (0° to 80°)	Electrical coil heater	Universidad of the Basque Country (Spain)	[27]
Monochromator (thermal detector)	0.8–2.2	473 to 1273	Normal	Cast iron plate heater	Henan Normal University (China)	[39]
FTIR	1.3–29	Up to 1400	Directional (0° to 60°)	Ceramic heater	Harbin Institute of Technology (China)	[43]
FTIR	2–25	1073 to 1873	Normal	Flame torch/ tubular furnace	Nanjing University of Science and Technology (China)	[44]
Monochromator (photon detector)	2–15	473 to 1003	Directional (N/A)	Electrical coil heater	National Institute of Metrology (China)	[51]
Spectroradiometer	0.6–40	1300 to 2500	Directional (0° to 80°)	Solar furnace	PROMES-CNRS (France)	[52]
FTIR	8–14	173 to 213	Normal	Refrigerator (cooling)	Chinese Academy of Sciences (China)	[53]
FTIR	1.4–26	550 to 1250	Normal	Laser heating	University of West Bohemia (Czech Republic)	[54,55]
FTIR	5–25	325 to 405	Normal	Solar-like halogen lamp	Brown University (USA)	[56]
FTIR	2–9	Up to 973	Normal	Electrical heater	University of Wisconsin-Madison (USA)	[57]
FTIR	0.7–29	773 to 1273	Normal	Blackbody radiator	Ruhr-University Bochum (Germany)	[58,59]
FTIR	0.8–8	1000 to 1700	Normal	Oxygen-gas flame	Tohoku University (Japan)	[63,64]
FTIR	1.5–20	Up to 2226	Normal	Oxy/acetylene torch	Advanced Fuel Research Inc. (USA)	[67]
FTIR	5–12	253 to 373	Normal	Circulating fluid	National Research Laboratory of Metrology (Japan)	[68]
FTIR	1.6–22	373 to 1673	Normal	Tantalum wire heater	Tokai University (Japan)	[69]
FTIR	2.5–25	323 to 773	Directional (0° to 50°)	Electrical heater	Korea Research Institute of Standards and Science (South Korea)	[70]
FTIR	0.6–15	773 to 1623	Normal	Electrical heater	Bundeswehr University of Munich (Germany)	[71]
FTIR	1–25	373 to 1473	Normal	Electrical heater	University of Duisburg-Essen (Germany)	[72]

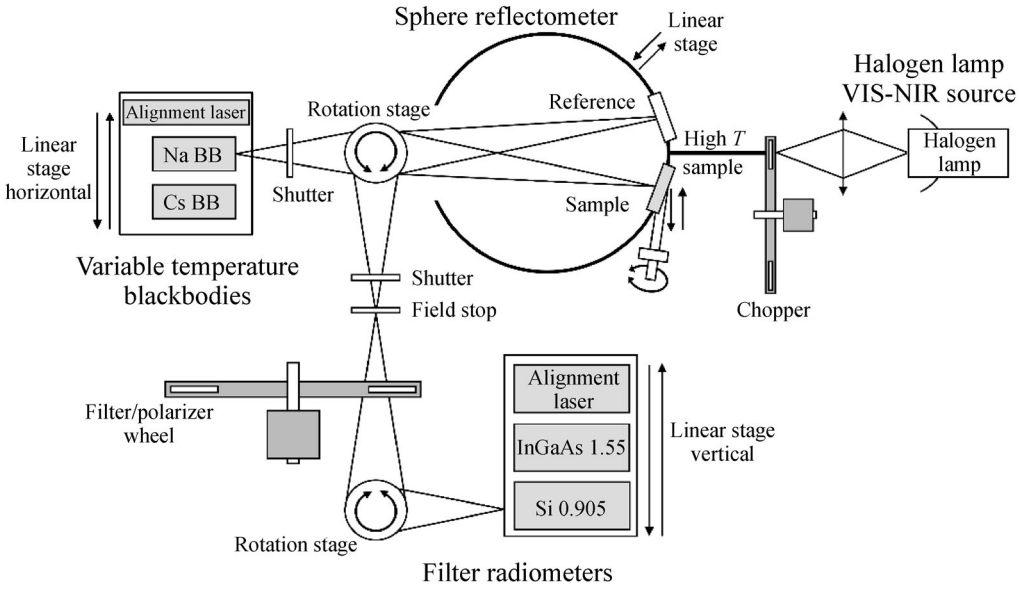

Fig. 7 Schematic with details of the indirect measurement method at NIST (reprinted from Ref. [28] with permission).

samples at high temperatures. Using the reciprocity principle [35], the directional-hemispherical reflectance is equal to the hemispherical-directional reflectance and can be used to obtain the emittance based on Eq. (10). As explained previously, by removing the integrating sphere using a linear translational stage, the radiation emitted from the sample is measured with a filter radiometer and compared with the blackbody signal to determine the surface temperature. The temperature measurement uncertainty can be reduced to within about 0.6 K at temperatures up to 1100 K [28].

Lee et al. [41] used an integrating sphere to measure the emittance (by measuring the directional-hemispherical reflectance) of silicon wafers with anisotropic roughness. Zhang et al. [29] developed a facility that uses a monochromator and an integrating sphere to measure the directional-hemispherical reflectance of samples heated by a cylindrical furnace up to 900 K. They measured the spectral emittance for 0.4 μm$\leqslant\lambda\leqslant$10 μm of selective coatings for CSP application. Fu et al. [73] constructed an indirect emittance measurement system using a hemispherical heating source and placed the sample at the center of the base of the hemisphere. The heating source is made of a quartz lamp array with reflecting walls to produce a nearly diffuse irradiation on the sample surface. A multiband spectrometer is used to measure the directionally reflected radiation from the sample through the opening on the top of the hemisphere. Both the sample temperature and emittance at wavelengths from 1.15 μm to 1.60 μm are deduced through a data analysis algorithm using two heating conditions that produces similar total intensities but with different spectral distributions.

An optical fiber reflectometer, coupled with a solar concentrator, has been developed for characterizing solar absorber materials for CSP technologies [74–76]. The facility, DISCO (derived from French meaning solar facility for optical characterization), is used to measure the total hemispherical reflectance weighted over the solar spectrum for relatively diffuse surfaces. As shown in Fig. 8, concentrated solar irradiation from a heliostat is focused on to the inlet of an optical fiber and is subsequently directed toward the sample at near-normal incidence. Seven optical fibers distributed angularly from 10° to 70°, with an interval of 10°, are connected to thermopiles to measure the directionally reflected radiation at prescribed collection angles. Bidirectional reflectance is thus determined at specified angles. The directional-hemispherical reflectance is then obtained by integration over all angles using the trapezoidal rule with extrapolation. This is a good approximation if the sample surface is relatively diffuse and isotropic in the azimuthal angle. The normal solar absorptance is calculated from the reflectance, since the light source comes directly from the sun. Using an electrical heater with a temperature controller, the sample

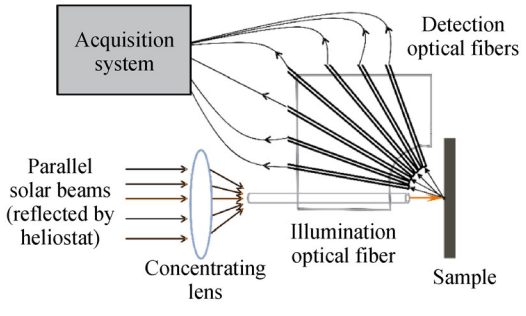

Fig. 8 Solar facility for optical properties characterization at PROMES laboratory (reprinted from Ref. [76] with permission).

may be heated up to 1000°C [74]. The total solar absorptance in the near-normal direction is measured without using a spectrometer. Since only seven fibers are used to collect the reflected radiation, this setup is not suitable for angular selective surfaces.

Wang et al. [77] developed an FTIR fiber-optic technique for measuring the specular reflectance of metamaterials as shown in Fig. 9. Since the feature size of the patterned structures is much smaller than the wavelength, the surface reflects in the specular direction only. Using a fiber coupler, the optical fiber can direct the radiation from the FTIR source to the sample at normal incidence in the VIS and NIR region from a wavelength of 0.4 μm to 2.0 μm. The probe fiber produces a 4-mm-diamter beam spot on the sample surface with collimating and focusing optics. Afterward, the same probe collects the normally reflected signal, which is finally acquired by the FTIR detector through the fiber coupler. The sample is mounted on a copper disk inside a heater assembly with a temperature controller for measuring temperatures up to 350°C. The same group also used an infrared microscope coupled to an FTIR spectrometer to measure the specular reflectance and transmittance of micro/nanostructures patterned on a semi-transparent substrate with a beam spot size of 40 μm × 40 μm at room temperature [78]. The emittance is then determined from Kirchhoff's law by subtracting the reflectance and transmittance from unity.

4 Application in energy conversion

Micro/nanostructures enable designed radiative properties for CSP and TPV applications. Four typical micro/nanostructures are reviewed in this section: multilayers, microcavities, metamaterials, and photonic crystals (PhC). The basic concepts are introduced, followed by reviews of representative fabricated structures and measurement results with a focus on high-temperature energy conversion applications.

4.1 Overview of micro/nanostructures for tuning radiative properties

4.1.1 Multilayers

Multilayer thin films have been widely used with required optical properties for a long time. Wang et al. [25] demonstrated a dielectric layer sandwiched between a metal film and a metal substrate for thermal emission control. For selective solar absorbers and TPV emitters, alternating dielectric and metal layers are often applied as shown in Fig. 10(a). The metallic layers in such an interference stack can increase the absorption of incident radiation, usually in a relatively short wavelength band, while reflecting longer wavelength radiation in a manner similar to a metal surface. Various oxides, nitrides, carbides, and other compounds, including cermet that is made of metallic nanoparticles dispersed in a dielectric matrix, can form multilayer structures using a variety of physical vapor and chemical vapor deposition techniques. The combination of absorption and interference effects can profoundly modify the absorption/emission spectrum with suitable selectivity for use as emitters in a TPV system [4] and solar absorbers in a CSP system [79].

4.1.2 Periodic gratings and microcavities

The periodic grating structures and microcavities, as illustrated in Fig. 10(b) for a microcavity structure, are useful for modifying both the directional and spectral radiative properties. Consider a plane wave incident from vacuum to the grating. When the plane of incidence is perpendicular to the grooves, the optical characteristics of a 1D surface-relief grating is described by the simple grating equation, according to the Floquet-Bloch theory [16],

$$\sin\theta_j = \sin\theta_{\text{inc}} + \mathrm{j}\frac{\lambda}{\Lambda}, \tag{11}$$

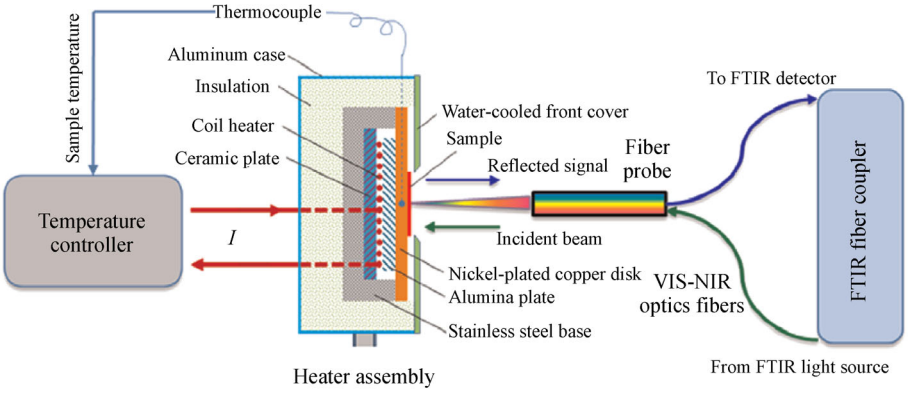

Fig. 9 Experimental setup for characterizing spectral normal optical properties with FTIR fiber optics technique at elevated temperatures (reprinted from Ref. [77] with permisssion).

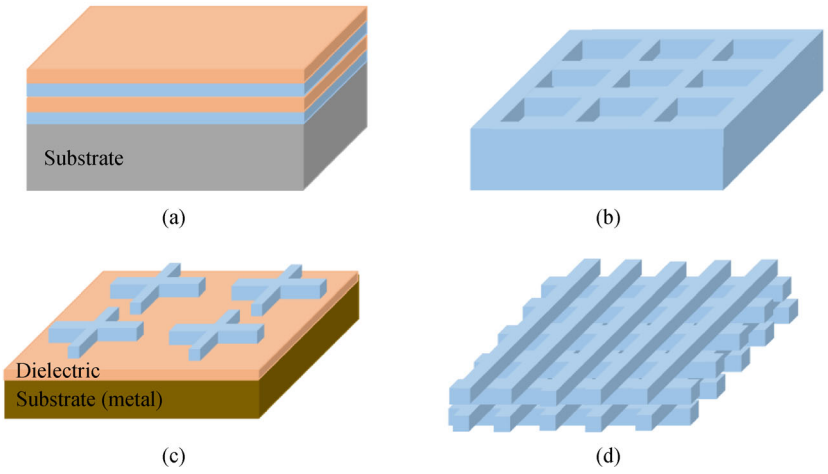

Fig. 10 Illustration of different micro/nanostructures.
(a) Multilayer structure; (b) 2D microcavity structure; (c) 2D metamaterial structure; (d) 3D PhC structure.

where θ_{inc} is the incidence angle, Λ is the period of grating, and θ_j is the diffraction angle for the jth diffraction order. For metallic gratings, when the incident wave is transverse magnetic (p-polarized), surface plasmon polariton (SPP) resonance occurs when the wavevector of a particularly diffracted wave is nearly parallel to the interface [80]. Similarly, for a polar dielectric material in the phonon absorption band, surface phonon polaritons (SPhPs) may be excited. The excitation of a SPP/SPhP resonance gives rise to surface electromagnetic wave that greatly enhances absorption. Consequently, thermal emission is also enhanced at the particular wavelength and direction of resonance. In the spectral region where these surface modes are not excited, the surface behaves similarly to a metallic surface with a low emittance.

Gratings also support resonance modes called optical cavities or waveguide modes, especially with deep gratings [4,18,60]. Magnetic polaritons (MPs) may also be excited to enhance absorption, and the resulting absorption peak is insensitive to the direction [18,31,40]. However, 1D grating structures support MP resonances only for TM waves. When cavity resonances are excited, microcavities with 2D gratings boost the absorptance or emittance due to the enhanced density of states [62–66]. The resonance wavelengths of the cavity modes (for both TE and TM waves) must satisfy [62,81]

$$\lambda(m,n,p) = 2\left[\left(\frac{m}{a}\right)^2 + \left(\frac{n}{b}\right)^2 + \left(\frac{p}{2h}\right)^2\right]^{-1/2}, \quad (12)$$

where a and b are the lateral dimension, and h is the depth of the cavity. The indices are m and $n = 0, 1, 2, \ldots$, and $p = 0, 1, 3, \ldots$ (odd number only). At least two indices must be nonzero. The localized cavity modes are usually not sensitive to the incident directions. Due to the 2D symmetric geometry, the radiative properties are independent of the polarization in the normal direction and weakly dependent on the polarization at other angles. SPPs may also be observed, but the excitation condition for SPPs depends on the period rather than the cavity geometry. Furthermore, SPPs are very sensitive to the incidence angle. Sai et al. [81] provided a detailed analysis of the effects of SPPs and microcavity modes in 2D tungsten microcavities on the spectral and directional radiative properties for TPV applications.

4.1.3 Metamaterials

A metamaterial is an engineered material with exotic characteristics that are often not readily available in naturally occurring materials. Electromagnetic metamaterials typically exhibit magnetic response at optical frequencies, which is not common in conventional materials. Some metamaterials use a thin dielectric film sandwiched between a patterned metal film and a metal substrate as shown in Fig. 10(c). The periodic patterned structures are an array of 1D long strips, 2D squares, 2D disks, or other shapes. The period of the pattern is usually smaller than the wavelengths of interest. Such metamaterials enable resonances in the visible and near-infrared range and are easier to fabricate than grating structures [10,15]. The excitation of a magnetic polariton is manifested by a strong enhancement in the time-varying magnetic field in the dielectric layer right below the metallic structures, with oscillating antiparallel currents above and below the dielectric layer [18,50,78]. MP resonances have been used for tuning radiative properties [82,83]; and the wavelength of the MP resonance (fundamental mode) may be predicted by an inductor-capacitor (LC) circuit model [84,85], which helps the design of the geometric structure and materials selection of metamaterials. The metal pattern can be designed into a variety of shapes with the same or different sizes to excite resonance at desired wavelength(s). Metamaterials have

the potential to realize broadband or narrowband emission/absorption at the wavelength region from the visible to the mid-infrared for high-temperature TPV emitter or solar absorber [15,82,86].

4.1.4 Photonic crystals

A photonic crystal is a periodic array of unit cells containing two or more materials, which replicate infinitely into one, two, or three dimensions. Figure 10(d) illustrates a 3D PhC with a woodpile structure [16]. There are numerous ways to construct photonic crystals. Sometimes it is difficult to classify a particular structure since it may belong to more than one category. For example, a 1D PhC is essentially a multilayer structure with alternative materials arranged periodically. Some 2D PhCs use microcavities or 2D gratings. They can be analyzed using the well-established PhC theory or with a numerical solver of Maxwell's Equations [17]. The physical significance of a PhC is that light may be confined or rejected by a photonic crystal similar to electrons in a real crystal. There exist passbands and stopbands in a particular PhC that can be used to modify radiative properties. Typically, the period of a PhC is 0.1–0.3 of the wavelength of interest for the PhC to exhibit distinct properties from the bulk counterparts. Promising results have been demonstrated by researchers using metallic PhCs with tungsten [87] or tantalum [88] microcavities as high-temperature TPV or solar TPV emitters. In addition to the geometric arrangement, the atomic structure of the constituent materials affects the characteristic spectra of PhC. Furthermore, the materials must be chemically stable at operating temperatures. Lee et al. [89] showed that surface electromagnetic waves coupled with a truncated 1D PhC made of alternative dielectric layers can produce coherent thermal emission for both polarizations.

4.2 Selective high-temperature solar absorbers

A solar absorber not only absorbs radiation from the sun but also emits a significant amount of radiation (mainly infrared) to the surroundings when operating at elevated temperatures. For the CSP application, the temperature of the solar absorber may be above 1000 K [6] and the blackbody emission spectrum at the surface temperature of the absorber does not coincide with the solar spectrum as shown in Fig. 11. To enhance the energy harvesting efficiency, a selective high-temperature solar absorber is required to absorb solar radiation as much as possible and emit thermal radiation as little as possible at longer wavelengths. Therefore, the ideal absorber has an absorptance/emittance value of unity in the main solar spectrum and zero at longer wavelength as illustrated in Fig. 11, though the exact cutoff wavelength depends on a number of factors [15].

The thermal transfer efficiency of a solar absorber $\eta(T_a)$ represents the fraction of sunlight captured minus the loss by emission to the (cold) surrounding [8,76]

$$\eta(T_a) = \alpha_s(T_a) - \frac{\overline{\varepsilon}(T_a)\sigma T_a^4}{C_f G_0}, \tag{13}$$

where $\alpha_s(T_a)$ is the hemispherical solar absorptance of the surface at temperature T_a, $\overline{\varepsilon}(T_a)$ is its total hemispherical emittance, C_f is the solar concentration factor, and G_0 is the total solar irradiance. The solar absorptance can be expressed as

$$\alpha_s(T_a) = \frac{1}{G_0}\int_0^\infty \alpha_\lambda(\lambda,T_a)G_\lambda(\lambda)\mathrm{d}\lambda, \tag{14}$$

where $\alpha_\lambda(\lambda,T_a)$ is the spectral absorptance of the surface at temperature T_a, and $G_\lambda(\lambda)$ is the spectral solar irradiance. The total solar irradiance can be integrated from the spectral solar irradiance by

$$G_0 = \int_0^\infty G_\lambda(\lambda)\mathrm{d}\lambda. \tag{15}$$

The integrations in Eqs. (14) and (15) need only to be carried out over 0.28 μm$\leqslant\lambda\leqslant$4.0 μm using a suitable solar irradiance spectrum, such as for an air mass coefficient AM1.5 [15]. The total, hemispherical emittance $\overline{\varepsilon}(T_a)$ is obtained from Eq. (6) using the surface temperature T_a.

For CSP applications, an ideal selective solar absorber requires a high absorptance ($\alpha_\lambda>0.93$) in the main solar spectrum (0.3–1.8 μm) and a low thermal emittance ($\varepsilon_\lambda<0.05$) in infrared region (1.8–25 μm), as shown in Fig. 11. Depending on the concentration factor and surface temperature, the cutoff wavelength $\lambda=1.8$ μm may be tuned to optimize the thermal transfer efficiency. This section introduces some measured results of micro/nanostructured solar absorbers suitable for CSP applications, focusing on multilayer, metamaterial, and PhC absorbers. Note that this paper is not intended to cover all types of selective solar absorbers. Comprehensive literature reviews can be found from Refs. [1,8,9,15].

4.2.1 Multilayer absorbers

Several direct emittance measurements [90–92] have been conducted on multilayer solar absorbers based on the apparatus shown in Fig. 2 [27]. The samples are made of different multilayer structures on stainless steel substrates and the measured temperature ranges from 150°C to 600°C. The sample used in Ref. [90] consists of a 53-nm top SiO_2 layer on two cermet layers, each with a thickness of 80 nm, made of Mo nanoparticles inside SiO_2 with different filling ratios, and then a 250 nm Ag layer (which can be treated opaque to radiation). Between the Ag layer and the stainless steel substrate is a thermally grown oxide. The sample used in Ref. [91] has a similar structure with

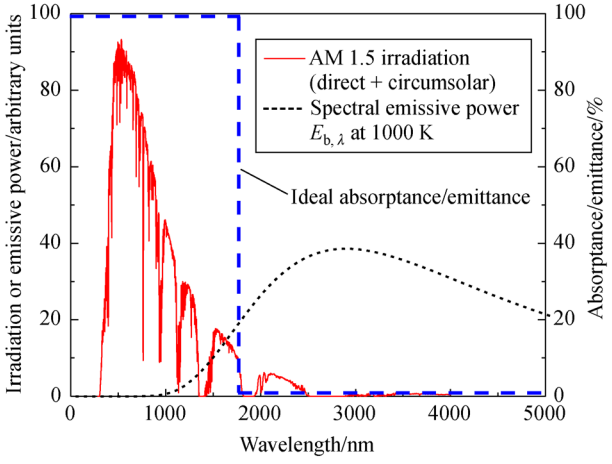

Fig. 11 Representative spectra for the spectral solar irradiance (AM1.5), blackbody emissive power at 1000 K, and the "ideal" absorptance/emittance spectrum for a solar absorber.

Si_3N_4 and cermet layers made of Mo:Si_3N_4, instead of SiO_2. The samples used in Ref. [92] is composed of Al_2O_3 (62 nm), WAlON (40 nm), WAlN (40 nm), and W (125 nm) films on a stainless steel substrate. The high-temperature direct measurement results have been compared with those obtained from the indirect method at room temperature. Generally speaking, the results from these studies suggest that, even with a small temperature dependence of the spectral emittance at $\lambda > 4$ μm, the total emittance calculated from Eq. (6) using the room-temperature spectral emittance can cause unacceptable error at elevated temperatures [91]. Therefore, it is important to measure the spectral emittance at operating temperatures. The indirect measurement results at room temperature should only be used to calculate the total emittance at a high temperature if the spectral emittance is independent of the temperature in a broad spectral region; a criterion that is hardly satisfied with real materials. Furthermore, the emittance may depend on the heating cycles and thermal stability becomes very important to high-temperature operation [92].

Indirect method has also been used to study solar absorptance and thermal emittance of multilayer structures, using a UV/VIS/NIR spectrophotometer and an FTIR spectrometer for the spectral ranges of 0.25–2 μm and 1.25–25 μm, respectively [76,93]. A spectrophotometer is a dispersive instrument that uses grating monochromators to separate the different colors (wavelength bands) and photon detectors. During the measurement, a sample heater can be used to heat the temperature up to 550°C. Soum-Glaude et al. [76] deposited $TiAlN_x/TiAlN_y/Al_2O_3$ coatings, with a total thickness from 150 to 206 nm, on stainless steel as selective CSP absorbers. They measured the near-normal ($\theta = 8°$ in the spectrophotometer and 10° in FTIR measurements incidence) spectral reflectance at different temperatures and used the indirect method to calculate the solar absorptance and thermal emittance (by neglecting the angular dependence). Their results show that the reflectance spectra are very similar from 20°C to 500°C, suggesting that the room temperature spectral absorptance/emittance can be used for calculating the solar absorptance and thermal emittance. The best performing sample has $\alpha_s = 0.93$ and $\overline{\varepsilon} = 0.22$ at the measured temperature of 550°C. In addition, they conducted hemispherical solar absorptance measurement under natural solar irradiation using the DISCO facility described previously in Fig. 8 and the results are in agreement with that obtained from the spectrophotometer. Jyothi et al. [93] used the same set of instruments to characterize multilayer titaniferous coatings on a stainless steel substrate at high temperatures from 80°C to 500°C. They observed that the total emittance increases from about 0.15 to 0.27 as the temperature increased from 200°C to 500°C, due to the increase in spectral emittance toward shorter wavelengths. The measured solar absorptance is 0.93, which reduces to about 0.90 after high-temperature measurement cycles. Annealing at temperatures greater than 550°C in air causes significant reduction in the solar absorptance [93]. Chen et al. [94] achieved very high solar absorptance with Ti/SiO_2 cascade optical cavities.

More recently, Li et al. [95] proposed an all ceramic TiN/TiNO/ZrO_2/SiO_2 absorber, as shown in Fig. 12(a), having selective absorptance and great thermal stability. The specular reflectance was measured using a UV/VIS/NIR spectrophotometer and an FTIR at wavelengths from 0.3 μm to beyond 15 μm at room temperature. The near-normal spectral absorptance can be deduced using the indirect method, as shown in Fig. 12(b). The measured results indicate that the selective solar coating exhibits a high absorptance in the wavelength range of 0.3–1.8 μm, with some variations due to interference effects. The spectral absorptance (or emittance) decreases sharply when the wavelength exceeds 1.8 μm. This selective coating has an excellent performance since the absorptance spectrum is very similar to the ideal curve shown in Fig. 11. Moreover, Fig. 12(b) also shows that the absorber sustains high solar absorption even after 150 h annealing at 1000 K. The integrated solar absorptance is 92%. By assuming that the spectral emittance is independent of temperature, a total emittance at 1000 K is 0.17. Clearly, such all-ceramic multilayers are promising as selective absorbing coatings with excellent stability. The temperature-dependence on the spectral absorptance/emittance deserves further investigation. Table 2 summarizes selective solar absorbers using different structures and materials, as well as the measurement instruments and performance.

4.2.2 Metamaterial, 2D PhC, and microcavity selective absorbers

Chang et al. [96] fabricated a refractory metamaterial solar

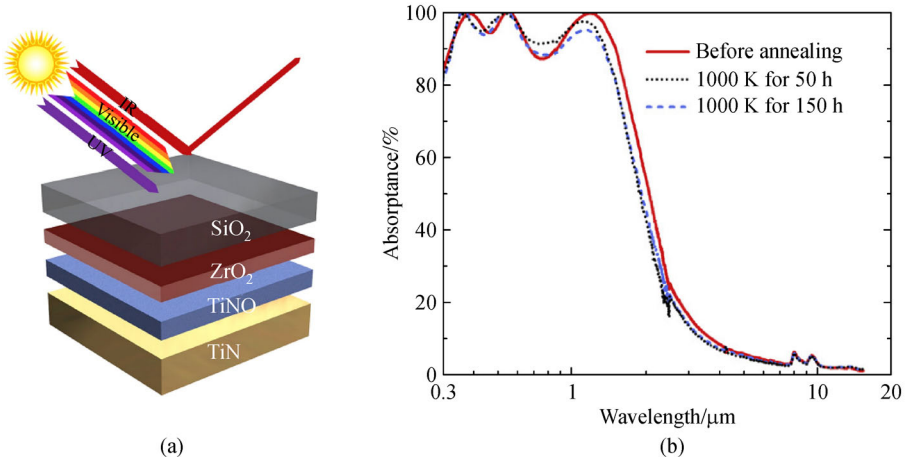

Fig. 12 Spectral absorptance of an all-ceramic solar selective absorber.
(a) 3D schematic of the all-ceramic TiN/TiNO/ZrO_2/SiO_2 four-layer structure; (b) measured absorptance spectra of the all-ceramic solar selective absorber before and after annealing at 1000 K (adapted from Ref. [95] with permission).

Table 2 Summary of spectral selective solar absorbers

Structure	Materials	Method and instrument	Directionality	Wavelength /μm	Temperature /K	Solar absorptance	Thermal emittance*	References
Multilayer	$TiAlN_x$/$TiAlN_y$/Al_2O_3	Indirect (spectrophotometer and FTIR)	Near-normal (8° or 10°)	0.25–25	298 to 823	0.93	0.22 (823 K)	[76]
Multilayer (cermet)	SiO_2/20%Mo:SiO_2/ 50%Mo:SiO_2/Ag	Direct (high accurate radiometer)	Normal	1.5–25	423 to 873	0.9	0.02 (298 K)	[90]
Multilayer (cermet)	Si_3N_4/20%Mo:Si_3N_4/ 37%Mo:Si_3N_4/Ag	Direct (high accurate radiometer)	Normal	1.5–25	523 to 873	–	0.15 (300 K)	[91]
Multilayer	W/WAlN/WAlON/ Al_2O_3	Direct (high accurate radiometer)	Directional (10° to 90°)	2–25	290 to 773	0.958	0.08 (355 K)	[92]
Multilayer	TiAlC/TiAlCN/TiAlSiC/ TiAlSiCO/TiAlSiO	Indirect (spectrophotometer and FTIR)	Near-normal (8° or 10°)	0.25–25	353 to 773	0.96	0.15 (773 K)	[93]
Multilayer	Ti/SiO_2 cascade optical cavities	Indirect (VIS/NIR spectrometer)	Near-normal	0.4–1.7	Room temperature	0.98	–	[94]
Multilayer	TiN/TiNO/ZrO_2/SiO_2	Indirect (spectrophotometer and FTIR)	Near-normal	0.3–15	Room temperature	0.922	0.17 (1000 K)	[95]
Metamaterial	Ti/MgF_2/W	Indirect (FTIR)	Near-normal	0.4–20	298 to 623	0.9	0.2	[77]
Metamaterial	W/Al_2O_3/W	Indirect (spectrophotometer)	Near-normal	0.3–2.5	293 to 1473	0.83	–	[96]
PhC	HfO_2 coated Ta 2D PhC	Indirect (FTIR)	Near-normal	0.3–3	Room temperature	0.86	0.26 (1000 K)	[99]
PhC	Al_2O_3 coated Ni nanopyramid array	Indirect (spectrophotometer and FTIR)	Near-normal	0.3–10	Room temperature	0.95	0.1 (298 K)	[100]
Gratings /microcavities	W cylindrical cavities or 2D pyramid gratings	Indirect (spectrophotometer and FTIR)	Near-normal	0.2–4.25	Room temperature	0.82 or 0.93	0.09 (800 K) or 0.17 (800 K)	[101]

Note: *—Parentheses show the temperature at which the total emittance is evaluated.

absorber, or a metasurface, based on a $W/Al_2O_3/W$ structure, as shown in Figs. 13(a) and 13(b). The unit cell of the pattern above the Al_2O_3 film has four tungsten nanodisks with diameters (d_1 = 140 nm, d_2 = 80 nm, d_3 = 60 nm, d_4 = 100 nm). The thickness of the Al_2O_3 layer and the nanodisks is 50 nm. The tungsten ground plane having a thickness of 150 nm is deposited on a Si substrate. The metamaterial structures can significantly enhance the absorption in the UV/VIS/NIR region due to the excitation of magnetic responses or MPs [82]. With different size distributions, the enhancement becomes much broader, as shown in Fig. 13(c). As the wavelength increases, the absorptance decreases rapidly around 1 μm and gradually approaches that of a plain film. The calculated solar absorptance is 0.83 based on the measured spectral absorptance at wavelengths of 0.3–1.5 μm. It should be emphasized that these structures are very stable and operate at temperatures close to 1200°C. They also performed spectral reflectance measurements at 1200°C using an in-house facility and demonstrated that the absorptance remains high in the wavelength region from 500 nm to 2000 nm [96]. The spectral peak can be shifted toward longer wavelengths by depositing a 20-nm-thick HfO_2 coating, as shown in Fig. 13(d). Other refractory metamaterials and geometries have also been used to achieve a high UV/VIS/NIR absorptance [97,98].

Wang et al. [77] developed a selective solar absorber based on $Ti/MgF_2/W$ metamaterial and used the fiber-optic FTIR spectrometer shown in Fig. 9 to characterize the spectral normal absorptance indirectly at temperatures up to 350°C. The unit cell of the Ti pattern contains a trapezoidal prism, whose top and bottom widths are 200 nm and 360 nm, respectively, with a height of 170 nm. The thickness of the MgF_2 film is 50 nm. The spectral absorptance barely changes with temperature in the measured temperature range. This structure demonstrates a high solar absorptance in a wide angular range, and the polarization has little effect. The high absorptance (>0.90) is due to the SPPs and MP resonances while the low infrared emittance (<0.20) is due to the high reflection from metal. In addition, the absorber efficiency could be further maximized through optimizing the geometry parameters for a given operating temperature.

Rinnerbauer et al. [99] fabricated a 2D PhC absorber/emitter for solar TPV application, targeting at an operating temperature of 1300 K. The 2D PhC design consists of cylindrical cavities (holes) etched into a tantalum (Ta substrate), which is a refractory metal with a high melting temperature (3017°C) and high corrosion resistance. A thin HfO_2 layer is coated on top of the PhC to add additional thermal stability as well as antireflection in the VIS/NIR region. Based on the indirect measurements at room

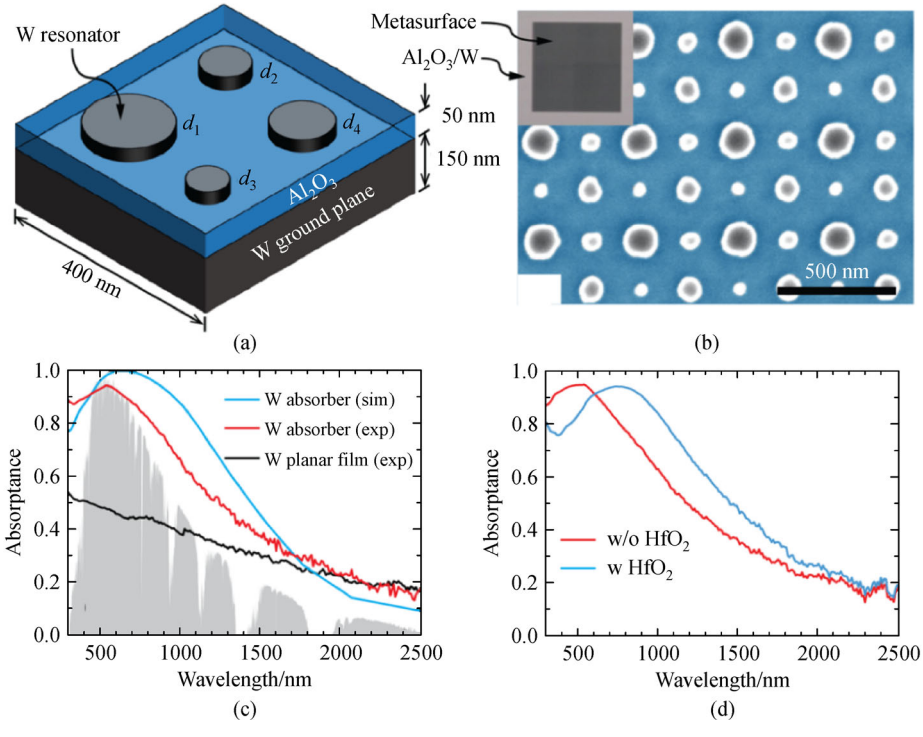

Fig. 13 Metamaterial solar absorber.

(a) A unit cell consisting of four W nanodisks, a Al_2O_3 spacer, and a W ground plane; (b) an SEM image (false colored) of the metasurface with an optical image on the upper-left corner; (c) simulated "sim" and measured "exp" absorptance of a W metasurface, along with that for a plain W film (The shaded background is the normalized AM1.5 solar spectrum.); (d) comparison of absorptance spectra between metasurfaces with and without a HfO_2 nanolayer (adapted from Ref. [96] with permission).

temperature, their results suggest that the metallic PhC could operate at about 1000 K as a solar selective absorber. Since the design is for the solar TPV application, further discussion will be given in Section 4.3.3. Li et al. [100] employed a template stripping method to fabricate nanophotonic structures made of nanopyramid arrays on a Ni surface, which is then coated with a Al_2O_3 film. This method may be used for cost-effective, large-scale production of high-efficiency selective solar absorbers. The absorptance/emittance is measured indirectly by a spectrophotometer at wavelengths of 0.3–15 μm at room temperature. The thermal stability of the fabricated samples is demonstrated by a comparison of the spectra before and after annealing at 800°C for 5 h. The solar absorptance of greater than 0.9 can be achieved with an infrared emittance of about 0.1. Note that this type of PhC structure may also be categorized as 2D gratings. It should be noted that earlier in 2003, Sai et al. [101] fabricated various 2D gratings or microcavities, such as square cavities, pyramid arrays, and cylindrical cavities on W films and demonstrated selective absorptivity for harvesting solar radiation both experimentally and theoretically. The measurement results and additional information for metamaterial and PhC absorbers are also included in Table 2.

4.3 Selective TPV emitters

As mentioned in the introduction, the TPV efficiency is constrained by sub-bandgap losses. A typical TPV cell has its own spectral external quantum efficiency (EQE) as shown in Fig. 14 for an InAsSbP cell with a low bandgap of 0.37 eV [5]. Even with an emitter temperature of 1500 K, approximately 35% of the thermal emission falls at wavelengths longer than that corresponding bandgap (i.e., 3350 nm). These photons cannot produce photocurrent and are converted to heat. A selective emitter having a higher emittance at frequencies above the bandgap and lower emittance at frequencies below the bandgap is a preferred choice [102]. In practice, the cutoff frequency can be at the location where the EQE drops sharply as illustrated in Fig. 14 for an ideal broadband selective emitter: $\varepsilon_\lambda = 1$ at shorter wavelengths when the EQE is high and $\varepsilon_\lambda = 0$ at longer wavelengths after the EQE approaches zero. An alternative design is to use a narrowband emitter with high emittance values near the peak of the EQE and lower emittance values at other wavelength. Such an ideal narrowband emitter is also shown in Fig. 14 and can be used to improve the conversion efficiency of TPV. The drawback of a narrowband emitter is that the power output may be significantly reduced. In practice, the bandwidth should be chosen to produce a sufficiently large short-circuit current. Hence, there is a tradeoff between output power and maximum efficiency [103]. Near-field TPV systems could provide high output power since the radiative heat flux is greatly enhanced [4]. Readers are referred to [104] for a recent review on near-field radiative energy conversion devices. In terms of angular dependence, in general, it is desired to have an emitter that is spectrally selective over a wide range of angles [4,102]. In addition, chemical and thermal stabilities at high temperatures are required for high-temperature TPV emitters, as for selective solar absorbers in CSP systems [9]. Similar to selective solar absorbers, periodic microstructures with high-temperature materials such as silicon, SiO_2, SiC, as well as refractory metals and their corresponding PhCs are the common choices for selective emitters.

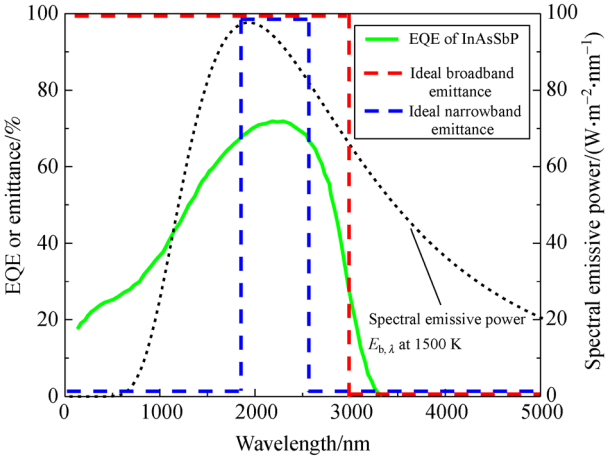

Fig. 14 Spectral EQE of an InAsSbP TPV cell, spectral emissive power of a blackbody at 1500 K, and the emittance spectra of ideal broadband and narrowband selective emitters.

4.3.1 Grating and microcavity emitters

Hesketh et al. [60,61] in the 1980s fabricated microgrooved silicon surfaces and measured their spectral emittance using a grating spectrometer for individual polarizations. However, the tunability is somewhat limited even with doped silicon. In the early 2000s, 2D tungsten grating [105], 1D SiC grating [106], and Cr-coated 2D silicon microcavities [107] have been developed for tuning the spectral radiative properties in the infrared. Sai et al. measured the emittance for various 2D gratings or microcavities, including reverse-pyramid Pt-coated silicon cavities [63,81] and rectangular tungsten microcavities with a period of 0.2–1.2 μm [81,108,109]. The SEM images of the reverse-pyramid (Pt-coated Si) cavities and tungsten rectangular microcavities are shown Figs. 15(a) and 15(b), respectively. Figure 15(c) shows the spectral emittance of the reverse-pyramid cavities with two periods, compared with a Pt film deposited on a polished Si surface. The microcavities can enhance the emittance, especially at the wavelengths near the period, suggesting SPPs are the main contribution to the enhanced emittance. In periodic structures made of Ag, Au, or Al, which are highly reflective, SPPs typically result in absorption peaks [16].

Table 3 Summary of spectral selective TPV emitters

Structure	Materials	Method and instrument	Directionality	Wavelength /μm	Temperature /K	Maximum normal emittance (wavelength location)	References
Periodic grating	Micro-grooved Si	Direct (spectrometer)	Directional (0° to 80°)	2–14	573 and 673	About 0.9 (3 μm)	[61]
Periodic grating	Tungsten 2D grating	Direct (FTIR)	Directional (0° and 30°)	1.0–5.0	1200	0.7 (1.6 μm)	[105]
Periodic grating	SiC 1D grating	Direct (FTIR)	Normal	9.5–13	773	0.9 (11.1 μm)	[106]
Microcavity	Pt-coated Si reverse-pyramid cavities	Direct (FTIR)	Normal	0.8–5	890	0.8 (1.6 μm)	[63]
Microcavity	Ti-coated Si rectangular cavities	Direct (spectrometer)	Normal	1–5	1073	0.8 (3.2 μm)	[65]
Microcavity	Ni rectangular cavities	Direct (spectrometer)	Normal	0.7–4	1000	0.95 (0.87 μm)	[66]
Microcavity	Cr-coated Si rectangular cavities	Direct (FTIR)	Directional (0° to 15°)	3–25	750	About 0.6 (6–10 μm)	[107]
Microcavity	W rectangular cavities	Direct (FTIR)	Normal	0.6–4	Up to 1400	0.8 (1.25 μm)	[108,109]
Microcavity	Perovskite-type manganese thermochromic materials	Indirect (FTIR)	Near-normal	1.25–25.5	173 to 373	0.95 (4 μm)	[111]
Microcavity	Ag-coated Si microcavities	Indirect (FTIR)	Near-normal	3.6–25	Room temperature	Near unity (8.87 μm, 5.63 μm, and 3.89 μm)	[112]
Microcavity	LSMO-coated silicon microcavity	Indirect (FTIR)	Near-normal	2.5–25	97 to 373	Near unity (6.5 μm)	[113]
Multilayer	Fabry-Perot cavity resonator	Direct (FTIR)	Directional (0° to 30°)	2–20	294, 600, and 800	About 0.8 (4.5 μm, 2.27 μm)	[25]
Metamaterial	Au-grating/SiO_2/Au on Si substrate	Direct (FTIR)	Directional (0° to 30°)	3.33–10	700 and 750	0.8 (7.69 μm), 0.6 (4.17 μm)	[50]
Metamaterial	SiC metasurfaces (2D-grooved)	Indirect (FTIR + microscope)	Near-normal	8–13	Room temperature	0.8 (12 μm)	[78]
Metamaterial	Pt-pattern/Al_2O_3/Pt on sapphire substrate	Indirect (FTIR + microscope)	Near-normal	0.8–3.5	Room temperature	Near unity (1.5 μm)	[114]
1D PhC	SiO_2/Si_3N_4 1D-PhC on Ag	Indirect (FTIR)	Directional (0°–80°)	0.85–1.1	Room temperature	0.6 (0.975 μm)	[117,118]
2D PhC	W cylindrical hole array	Indirect (FTIR)	Near-normal	1–3	Room temperature	Near unity (1.5 μm)	[87]
2D PhC	Ta cylindrical hole array	Indirect (FTIR)	Near-normal	1.4–3	Room temperature	Near unity (1.9 μm)	[88]
2D PhC	HfO_2-coated Ta cylindrical hole array	Indirect (FTIR)	Near-normal	0.3–3	Room temperature	Near unity (1.9 μm)	[99]
2D PhC	Ta-W alloy cylindrical hole array	Indirect (FTIR)	Near-normal	1.4–3	Room temperature	Near unity (2 μm)	[115,116]
3D PhC	Ni woodpile structure	Direct (FTIR)	Normal	2–14	600, 700 and 800	0.65 (3 μm)	[120]
3D PhC	Pt-coated silicon scaffold	Direct (FTIR)	Directional (0° to 75°)	1.8–10.2	889 and 939	Near unity (2.5 μm)	[122]

Microcavities in Pt can boost the emittance in the NIR at the temperature close to 900 K, though the emittance peaks are rather broad due to losses in Pt as shown in Fig. 15(c). The emittance spectra of three tungsten microcavities are shown in Fig. 15(d) along with that of plain tungsten at 1288 K, except for grating A, which is at 1164 K. The grating parameters for the three gratings are: grating A: Λ = 1.0 μm, a = 0.8 μm and h = 0.7 μm; grating B: Λ = 1.2 μm, a = 0.9 μm and h = 0.63 μm; and grating C: Λ = 1.2 μm, a = 0.90 μm and h = 0.78 μm, where a is the width and h is the depth of the cavity. A high emittance can be observed in the VIS and NIR regions mainly due to the cavity resonance modes, though SPPs also play a role at $\lambda \approx \Lambda$. These modes can be well predicted using Eq. (12), originally proposed by Maruyama et al. [107]. Clearly, metallic microcavities are suitable for TPV systems due to their selective emittance and high-temperature resistance. A variety of microcavities with different shapes and metal or coating materials have been fabricated and demonstrated with both broadband and narrowband emitters by many researchers [62,65,66,110–113]. More details are summarized in Table 3.

4.3.2 Multilayer, metamaterial, and PhC thermal emitters

The emissometer shown in Fig. 5 has been used to directly measure fabricated multilayer structures and metamaterials at elevated temperatures [25,50]. The structures and results are shown in Fig. 16 to explore the effects of polarization and direction on the spectral emittance.

Figure 16(a) shows the structure of an asymmetric Fabry-Perot cavity resonator, which mainly contains a SiO_2 optical cavity sandwiched between a thin Au film (d_f = 10 nm) and an opaque Au film (200 nm thick) deposited on a Si substrate [25]. The top 100-nm SiO_2 layer is for protection, while the Ti/Pt layers are for adhesion and act as a barrier to prevent Au from diffusing into Si at high temperatures. The emittance spectra for different polarizations at an emission angle of 30° are plotted in Figs. 16(b) and 16(c). There are emittance peaks

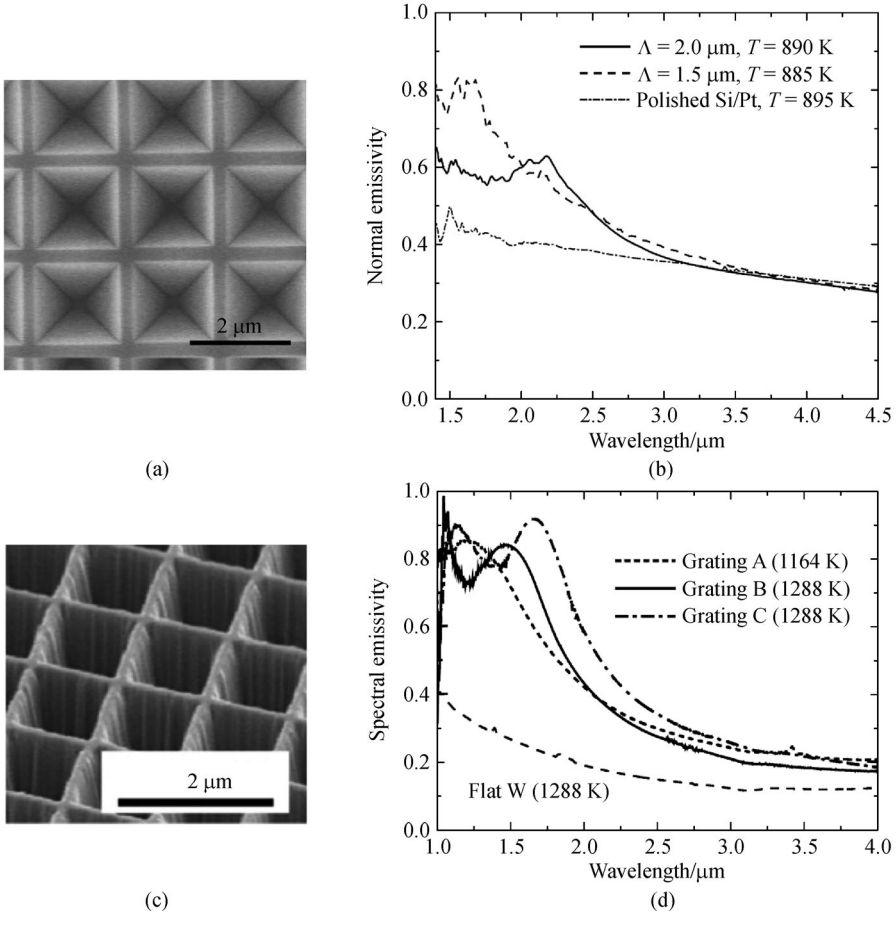

Fig. 15 Measured spectral emittance of microcavities.
(a) SEM image of Pt-coated Si reverse-pyramid microcavities; (b) SEM image of W rectangular microcavities; (c) emittance spectra of two reverse-pyramid samples, and that of flat Si coated with a Pt film; (d) emittance spectra of rectangular-cavity samples and a flat W in the normal direction (adapted from Ref. [81] with permission).

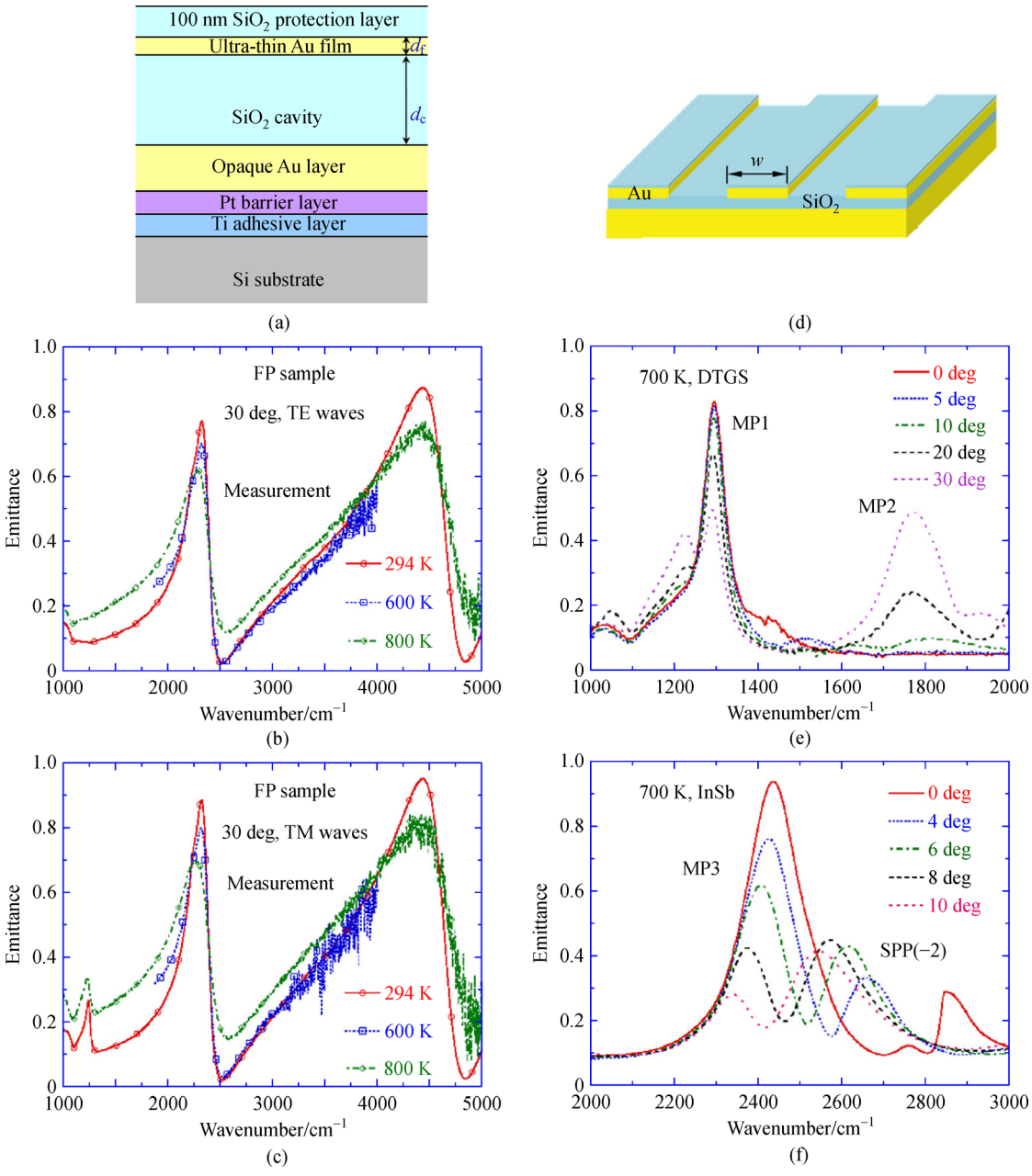

Fig. 16 (a) Schematic of the fabricated Fabry-Perot cavity resonator; (b) and (c) the emittance spectra for TE and TM waves, respectively, at different temperatures for $\theta = 30°$; (d) schematic of the metamaterial emitter made of a gold grating and SiO_2 spacer on an optically opaque Au film; (e) emittance measured with a DTGS detector; (f) emittance measured with an InSb detector for TM wave at 700 K for different zenith angles (adapted with permission from Ref. [25] for (a, b, c); and from Ref. [50] for (d, e, f)).

for both polarizations due to the resonance modes with d_c = 1.55 μm for SiO_2 optical cavity. Note that the spectrum at 294 K is measured with the indirect method. Different detectors are used in the FTIR for sample temperature of 600 K and 800 K as explained previously. In general, the emittance peaks become broader and the resonance frequencies slightly shift toward lower wavenumbers when the temperature increases from 294 K to 800 K. The resonance frequencies in oblique direction are higher than those in the normal direction because of the cosine term in the phase shift. The change of the resonance frequency with emission angles indicates the selectivity of spatial direction for metamaterials. There is an additional small emittance peak at 1250 cm^{-1} for TM waves only. The reason for this is that a canceling effect of the reflection coefficients at the air-SiO_2 and SiO_2-Au interfaces due to the unique optical constants of SiO_2 in this region [25].

The metamaterial structure is illustrated in Fig. 16(d), with a 1D Au grating patterned on a thin SiO_2 film that is deposited on an opaque Au film. A protection layer of SiO_2

covers the metamaterial. Since SPP and MP modes cannot be excited with TE waves, only the TM-wave emittance spectra are shown in Figs. 16(e) and 16(f) at 700 K for different emission angles θ. The room-temperature DTGS detector is used for wavenumber range of 1000–2000 cm^{-1} (10 – 5 μm), and a liquid-nitrogen-cooled InSb detector is used for 2000–3000 cm^{-1}. The Au grating has a period of 7 μm, a width of 3.5 μm, and a thickness of 170 nm. A large emission peak at 1296 cm^{-1} with a maximum of 0.82 at θ = 0° is identified as MP1 (the fundamental MP mode). The peak location is insensitive to the angle even at $\theta = 30°$, while the peak emittance decreases as θ increases. The reason for this is that the optical constants of SiO_2 changes abruptly in this region and introduce additional peaks when $\theta > 20°$. Another peak near 1800 cm^{-1} is caused by MP2 and only observable when $\theta > 15°$. At large wavenumbers, MP3 can also be observed as shown in Fig. 16(f) that can also be coupled with the SPP (–2 order). Due to the coupling, the resonance location is a strong function of the emission angle. The coupling between different plasmonic modes may be applied in optical detection and novel plasmonic devices.

Using an infrared microscope coupled to an FTIR spectrometer, Yang et al. [78] demonstrated a spectral emission peak, which is insensitive to the emission angle and polarization, with a SiC metasurface fabricated by focused ion beam etching. Due to the 2D grating structure, the MP modes can be excited by both polarizations, resulting in an emission peak in the mid-infrared region. Woolf et al. [114] fabricated a metamaterial with a cross-patterned Pt on top of a Al_2O_3 film deposited on a Pt ground plane. They measured the spectral emittance indirectly using a microscope coupled with an FTIR spectrometer and demonstrated a high emittance in the 1–2 μm wavelength range. Additional information can be found in Table 3.

There have been numerous studies on the fabrication and characterization of various PhCs for selective emitter applications. Metallic 2D PhCs have been fabricated with refractory metals, such as W [87], Ta [88], HfO_2 coated Ta [99], and Ta-W alloy [115,116], and tested at both room temperature and high temperatures. Some of these PhCs will be further discussed in the subsequent subsection. Lee et al. [117,118] demonstrated narrowband selective emission using truncated 1D PhCs on an opaque silver film using the indirect method. Moreover, 3D PhCs using a woodpile structure [119,120] and Si scaffold microstructures [121,122] have also been fabricated, and their emittance spectra have been measured directly at elevated temperatures. Additional information about PhC emitters and measurement results are summarized in Table 3.

4.3.3 Solar TPV application

A solar TPV uses concentrated solar energy to heat the TPV emitter from the opposite side and the emitter subsequently sends radiation to a PV cell. It is a power system that could potentially be used together with a concentrated solar system to replace the conventional power cycle. Therefore, a solar TPV is a hybrid CSP system using a PV generator. For a solar TPV system to be competitive, the temperature of the emitter/absorber needs to be above 1000 K, and typically, the area of the PV cell is much greater than that of the absorber. Therefore, it is desired to have a selective solar absorber on one side to increase the collection efficiency and a selective emitter on the other side to increase the TPV efficiency. Lenert et al. [11] designed a nanophotonic solar TPV system, with a multiwalled carbon nanotube absorber and a 1D Si/SiO_2 PhCs as the selective emitter, which has an overall conversion efficiency of 3.2% with a solar simulator.

Researchers at MIT developed and measured several metallic PhC-based emitters/absorbers for solar TPV applications [87,99]. The PhC structure is based on 2D cylindrical cavities (or holes) etched into W or Ta substrate, with different parameters, as illustrated by the SEM images in Fig. 17, along with the measured and calculated emittance spectra. The main features are summarized below. Figure 17(d) shows the measured and simulated normal emittance of two W-PhC samples through the indirect method at room temperature: Sample I: r = 0.48 μm, $\Lambda = 1.22$ μm, and h = 1.30 μm; Sample II: r = 0.55 μm, $\Lambda = 1.40$ μm, and h = 1.60 μm, with here, r, Λ, and h being the radius, period, and depth of the hole [87]. The measured and simulated resonant features agree reasonably well, considering the nonuniformity in the fabricated sample and variation of the optical constants. The oscillation is associated with the resonance effect in the PhC. These samples have a very high emittance at $\lambda < 2$ μm and a lower emittance at longer wavelengths. These results have been verified at high temperatures (> 1200 K) using a high-temperature emissometry with an electrical heater and a FTIR spectrometer.

A selective 2D PhC was fabricated on both sides of a flat Ta substrate with different geometries: one side as a solar absorber and the other as a TPV emitter, as shown in Figs. 17(b) and 17(c), respectively [99]. The Ta PhC is coated with a HfO_2 film. Figure 17(e) shows the measured and simulated emittance spectra of the PhC absorber (r = 0.24 μm, $\Lambda = 0.66$ μm, and h = 4.6 μm), emitter (r = 0.53 μm, $\Lambda = 1.28$ μm, and h = 7.0 μm), and a HfO_2-coated flat Ta absorber, measured at room temperature using the indirect method. Interestingly, the flat Ta with coating has some good selectivity, although the cutoff wavelength is too short (approximately 0.85 μm). With the PhC structure, the cutoff wavelength of the solar absorber is increased to > 1 μm to improve the collection efficiency. The emittance spectrum may be tailored by varying the structure size. Using a larger radius and depth, the cutoff wavelength is pushed to about 2 μm to match with the bandgap of the semiconductors (such as InGaAs or InGaSb) used in the PV cell [3–5]. The double-sided

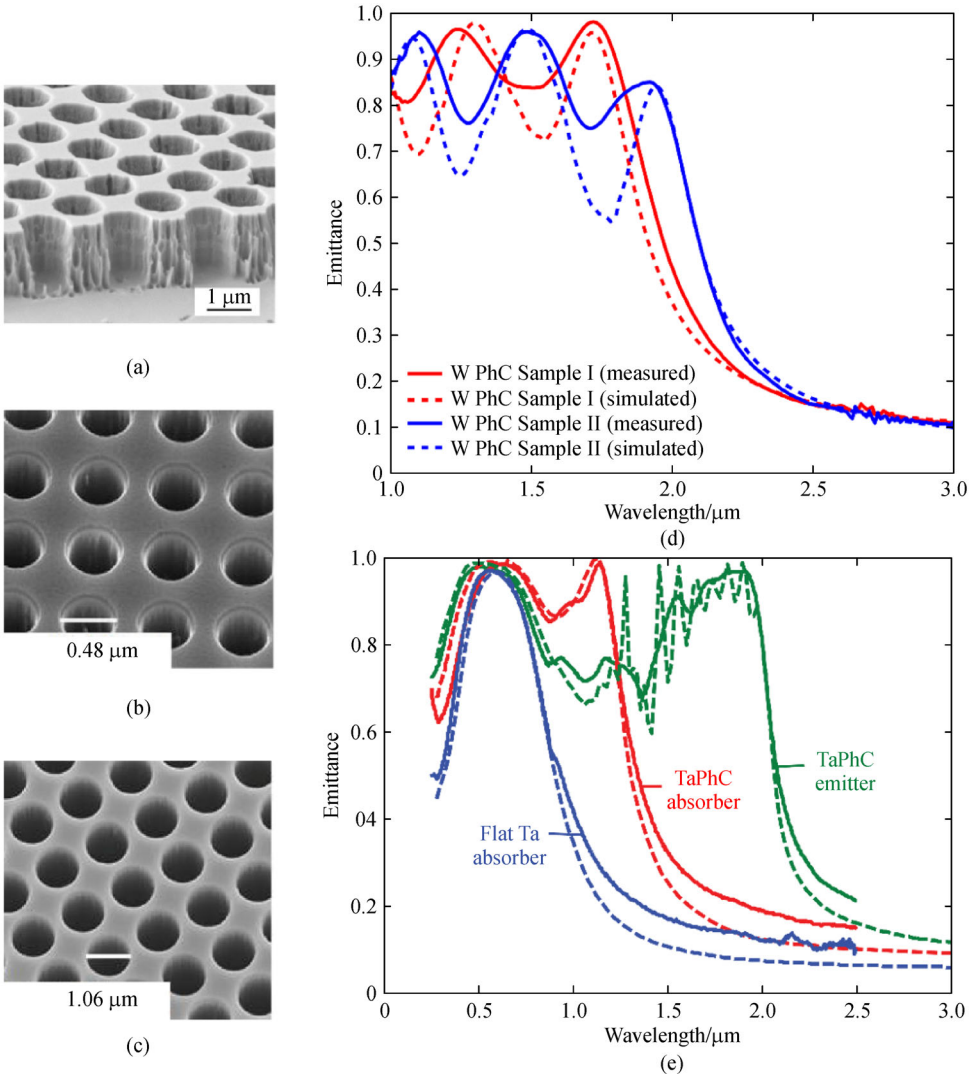

Fig. 17 SEM images.

(a) W PhC emitter; (b) Ta PhC absorber; (c) Ta PhC emitter; (d) measurement and simulated (near-normal) emittance spectra of W PhC; (e) measured (solid lines) and simulated (dashed lines) emittance spectra of the PhC emitter, PhC absorber, and a flat Ta absorber, all with a HfO_2 coating (adapted with permission from Ref. [87] for (a and d), and from Ref. [99] for (b, c, and e))

PhC material was tested in a solar TPV system with an InGaAsSb PV cell using a solar simulator at an irradiance of 60–130 kW/m^2 (i.e., concentration ratio C_f from 60 to 130). The measured system efficiency is 3.74% at an irradiance of 130 suns with an output power density of 0.49 W/cm^2. The measurements also show that at the same irradiance value, the system efficiency is 3.16% for a coated flat Ta absorber and 1.6% for a near-blackbody absorber using carbon nanotubes [99]. The system efficiency of an area optimized solar TPV with a near-blackbody absorber is twice the value of 1.6% [11], suggesting that the efficiency of the double-sided PhC solar TPV can be further improved.

Nam et al. [12] analyzed a solar TPV system with a 2D tantalum photonic crystal selective absorber/emitter, and numerically showed that the solar TPV efficiency of 10% could be achieved with a tandem filter at the emitter temperature of 1400 K. Shimizu et al. [13] fabricated a selective solar TPV absorber/emitter by depositing photonic multilayers on both sides of a planar 1-mm-thick tungsten substrate. Each of the photonic multilayers consists of a 15-nm tungsten film sandwiched between yttria-stabilized zirconia (YSZ) layers of varying thicknesses. The maximum system efficiency of 8% was observed at an operating temperature of 1640 K [13].

5 Conclusions and outlook

This paper reviews the state-of-the-art measurement facilities and instruments for emittance measurements of solids, focusing on the spectral directional emittance of

microfabricated surface structures. It also summarizes recent developments of micro/nanostructured materials for high-temperature CSP and TPV applications and measurement results, with an emphasis on multilayers, microcavities, metamaterials, and photonic crystals. This review is not meant to be exhaustive: only representative works are selected from the large body of publications related to this multidisciplinary topic. Nevertheless, it is hoped that researchers will find this review helpful in terms of the general methodology and underlying principles associated with the measurement techniques, structural designs, and materials selection. Some recommendations and possible future research directions are summarized as follows.

It is important to directly measure the spectral, directional emittance at the operating temperatures rather than using the room-temperature results, since most of the materials are subject to physical and chemical changes at elevated temperatures. High-accuracy emissometry facilities are still limited and may be difficult to access. While indirect measurements have been routinely done using commercial spectrophotometers and/or FTIR spectrometers, most of the measurements are performed at room temperature. High-temperature measurements using the indirect method may provide a practical alternative to the direct method.

It is imperative to develop high-temperature reference materials as emittance standard. While efforts have been devoted to the intercomparison of spectral emittance measurements by different laboratories, particularly national laboratories, challenges exist in maintaining the material stability and in interpreting measurement results from different laboratories due to their different instrument configurations. Moreover, directional measurements for individual polarizations are rather limited, though important for the characterization of micro/nanostructures.

Micro/nanostructures have been successfully fabricated and demonstrated with desirable spectral emittance characteristics using a combination of refractory metal, cermets, oxides, carbides, etc. Selected structures and materials have been tested with a good thermal and chemical stability. These structures should be further optimized for large scale applications. The spectral, directional emittance should be fully characterized.

At present, the obtained efficiency of solar TPV is still relatively low, making it hard to compete with conventional power plant integrated into CSP systems. The system efficiency may be boosted by using a narrow band emitter with a near-field TPV system.

In addition to selective surface absorbers, there are ongoing studies on the falling-particle receiver and heat-exchanger system for use as a potential CSP technology, where a fluidized bed with microscale ceramic particles is used as the solar absorber. It is important to measure the absorptance/emittance of these ceramic particle clusters or particles in the fluidized bed at elevated temperatures.

Acknowledgements This work was supported by the China Scholarship Council (No. 201806320236), the Academic Award for Outstanding Doctoral Candidates of Zhejiang University (No. 2018071), the Key Research and Development Program of Ningxia Hui Autonomous Region (No. 2018BCE01004), and the US Department of Energy's Office of Energy Efficiency and Renewable Energy (EERE) under the Solar Energy Technologies Office.

Notations

C_f	Solar concentration factor
C_1	First radiation constant
C_2	Second radiation constant
E	Emissive power/($W \cdot m^{-2}$)
E_λ	Spectral emissive power/($W \cdot m^{-2} \cdot \mu m^{-1}$)
G_0	Total solar irradiance/($W \cdot m^{-2}$)
G_λ	Spectral solar irradiance/($W \cdot m^{-2} \cdot \mu m^{-1}$)
I	Radiation intensity/($W \cdot m^{-2} \cdot sr^{-1}$)
I_λ	Spectral intensity/($W \cdot m^{-2} \cdot sr^{-1} \cdot \mu m^{-1}$)
T	Temperature/K

Greek symbols

α	Absorptance
ε	Emittance
η	Efficiency
θ	Zenith angle/(°)
Λ	Period of nanostructure/μm
λ	Wavelength/μm
ρ	Reflectance
σ	Stefen-Boltzmann constant
ψ	Azimuthal angle

Subscript

a	Absorber
b	Blackbody
θ	Directional
λ	Spectral

Abbreviation

CSP	Concentrating solar power
EQE	External quantum efficiency
FTIR	Fourier-transform infrared (spectrometer)
PhC	Photonic crystal
PV	Photovoltaic
TPV	Thermophotovoltaic(s)

References

1. Weinstein L A, Loomis J, Bhatia B, Bierman D M, Wang E N, Chen G. Concentrating solar power. Chemical Reviews, 2015, 115 (23): 12797–12838

2. Behar O. Solar thermal power plants—a review of configurations and performance comparison. Renewable & Sustainable Energy Reviews, 2018, 92: 608–627
3. Daneshvar H, Prinja R, Kherani N P. Thermophotovoltaics: fundamentals, challenges and prospects. Applied Energy, 2015, 159: 560–575
4. Basu S, Chen Y B, Zhang Z M. Microscale radiation in thermophotovoltaic devices—a review. International Journal of Energy Research, 2007, 31(6–7): 689–716
5. Ferrari C, Melino F, Pinelli M, Spina P R. Thermophotovoltaic energy conversion: analytical aspects, prototypes and experiences. Applied Energy, 2014, 113: 1717–1730
6. Turchi C S, Ma Z, Neises T W, Wagner M J. Thermodynamic study of advanced supercritical carbon dioxide power cycles for concentrating solar power systems. Journal of Solar Energy Engineering, 2013, 135(4): 041007
7. Romero M, Steinfeld A. Concentrating solar thermal power and thermochemical fuels. Energy & Environmental Science, 2012, 5 (11): 9234–9245
8. Bermel P, Lee J, Joannopoulos J D, Celanovic I, Soljacie M. Selective solar absorbers. Annual Review of Heat Transfer, 2012, 15(15): 231–254
9. Zhou Z, Sakr E, Sun Y, Bermel P. Solar thermophotovoltaics: reshaping the solar spectrum. Nanophotonics, 2016, 5(1): 1–21
10. Pfiester N A, Vandervelde T E. Selective emitters for thermophotovoltaic applications. Physica Status Solidi (A), Applications and Materials Science, 2017, 214(1): 1600410
11. Lenert A, Bierman D M, Nam Y, Chan W R, Celanović I, Soljačić M, Wang E N. A nanophotonic solar thermophotovoltaic device. Nature Nanotechnology, 2014, 9(2): 126–130
12. Nam Y, Yeng Y X, Lenert A, Bermel P, Celanovic I, Soljačić M, Wang E N. Solar thermophotovoltaic energy conversion systems with two-dimensional tantalum photonic crystal absorbers and emitters. Solar Energy Materials and Solar Cells, 2014, 122: 287–296
13. Shimizu M, Kohiyama A, Yugami H. High-efficiency solar-thermophotovoltaic system equipped with a monolithic planar selective absorber/emitter. Journal of Photonics for Energy, 2015, 5 (1): 053099
14. Rephaeli E, Fan S. Absorber and emitter for solar thermophotovoltaic systems to achieve efficiency exceeding the Shockley-Queisser limit. Optics Express, 2009, 17(17): 15145–15159
15. Khodasevych I E, Wang L, Mitchell A, Rosengarten G. Micro- and nanostructured surfaces for selective solar absorption. Advanced Optical Materials, 2015, 3(7): 852–881
16. Zhang Z M. Nano/microscale Heat Transfer. 2nd ed. Springer Nature Switzerland AG, 2020
17. Rinnerbauer V, Ndao S, Yeng Y X, Chan W R, Senkevich J J, Joannopoulos J D, Soljačić M, Celanovic I. Recent developments in high-temperature photonic crystals for energy conversion. Energy & Environmental Science, 2012, 5(10): 8815–8823
18. Zhang Z M, Wang L P. Measurements and modeling of the spectral and directional radiative properties of micro/nanostructured materials. International Journal of Thermophysics, 2013, 34(12): 2209–2242
19. Honner M, Honnerova P. Survey of emissivity measurement by radiometric methods. Applied Optics, 2015, 54(4): 669–683
20. Wang L P, Basu S, Zhang Z M. Direct and indirect methods for calculating thermal emission from layered structures with nonuniform temperatures. Journal of Heat Transfer, 2011, 133(7): 072701
21. Jones J M, Mason P E, Williams A. A compilation of data on the radiant emissivity of some materials at high temperatures. Journal of the Energy Institute, 2019, 92(3): 523–534
22. Monte C, Hollandt J. The measurement of directional spectral emissivity in the temperature range from 80°C to 500°C at the Physikalisch-Technische Bundesanstalt. High Temperatures. High Pressures, 2010, 39(2): 151–164
23. Monte C, Gutschwager B, Morozova S P, Hollandt J. Radiation thermometry and emissivity measurements under vacuum at the PTB. International Journal of Thermophysics, 2009, 30(1): 203–219
24. Cagran C P, Hanssen L M, Noorma M, Gura A V, Mekhontsev S N. Temperature-resolved infrared spectral emissivity of SiC and Pt-10Rh for temperatures up to 900°C. International Journal of Thermophysics, 2007, 28(2): 581–597
25. Wang L P, Basu S, Zhang Z M. Direct measurement of thermal emission from a Fabry-Perot cavity resonator. Journal of Heat Transfer, 2012, 134(7): 072701
26. Mercatelli L, Meucci M, Sani E. Facility for assessing spectral normal emittance of solid materials at high temperature. Applied Optics, 2015, 54(29): 8700–8705
27. del Campo L, Pérez-Sáez R B, Esquisabel X, Fernández I, Tello M J. New experimental device for infrared spectral directional emissivity measurements in a controlled environment. Review of Scientific Instruments, 2006, 77(11): 113111
28. Hanssen L M, Cagran C P, Prokhorov A V, Mekhontsev S N, Khromchenko V B. Use of a high-temperature integrating sphere reflectometer for surface-temperature measurements. International Journal of Thermophysics, 2007, 28(2): 566–580
29. Zhang Y F, Dai J M, Wang Z W, Pan W D, Zhang L. A spectral emissivity measurement facility for solar absorbing coatings. International Journal of Thermophysics, 2013, 34(5): 916–925
30. Fu C J, Zhang Z M. Thermal radiative properties of metamaterials and other nanostructured materials: a review. Frontiers of Energy and Power Engineering in China, 2009, 3(1): 11–26
31. Zhang Z M, Ye H. Measurements of radiative properties of engineered micro-/nanostructures. Annual Review of Heat Transfer, 2013, 16(1): 345–396
32. Dan A, Barshilia H C, Chattopadhyay K, Basu B. Solar energy absorption mediated by surface plasma polaritons in spectrally selective dielectric-metal-dielectric coatings: a critical review. Renewable & Sustainable Energy Reviews, 2017, 79: 1050–1077
33. Modest M F. Radiative Heat Transfer. 3rd ed. New York: Academic Press, 2013
34. Zhang Z M, Tsai B K, Machin G. Radiometric Temperature Measurements: I. Fundamentals; II. Applications. New York: Academic Press, 2009
35. Howell J R, Menguc M P, Siegel R. Thermal Radiation Heat Transfer. 6th ed. New York: CRC Press, 2015
36. Worthing A. Temperature radiation emissivities and emittances. Journal of Applied Physics, 1940, 11(6): 421–437
37. Ramanathan K, Yen S. High-temperature emissivities of copper,

aluminum, and silver. Journal of the Optical Society of America, 1977, 67(1): 32–38
38. Masuda H, Higano M. Measurement of total hemispherical emissivities of metal wires by using transient calorimetric technique. Journal of Heat Transfer, 1988, 110(1): 166–172
39. Zhang F, Yu K, Zhang K, Liu Y, Xu K, Liu Y. An emissivity measurement apparatus for near infrared spectrum. Infrared Physics & Technology, 2015, 73: 275–280
40. Yang P, Ye H, Zhang Z M. Experimental demonstration of the effect of magnetic polaritons on the radiative properties of deep aluminum gratings. Journal of Heat Transfer, 2019, 141(5): 052702
41. Lee H J, Bryson A C, Zhang Z M. Measurement and modeling of the emittance of silicon wafers with anisotropic roughness. International Journal of Thermophysics, 2007, 28(3): 918–933
42. Yang P, Chen C, Zhang Z M. A dual-layer structure with record-high solar reflectance for daytime radiative cooling. Solar Energy, 2018, 169: 316–324
43. Guo Y M, Pang S J, Luo Z J, Shuai Y, Tan H P, Qi H. Measurement of directional spectral emissivity at high temperatures. International Journal of Thermophysics, 2019, 40(1): 10
44. Ren D, Tan H, Xuan Y, Han Y, Li Q. Apparatus for measuring spectral emissivity of solid materials at elevated temperatures. International Journal of Thermophysics, 2016, 37(5): 51
45. Pérez-Sáez R B, Campo L, Tello M J. Analysis of the accuracy of methods for the direct measurement of emissivity. International Journal of Thermophysics, 2008, 29(3): 1141–1155
46. Honnerová P, Martan J, Honner M. Uncertainty determination in high-temperature spectral emissivity measurement method of coatings. Applied Thermal Engineering, 2017, 124: 261–270
47. Monte C, Hollandt J. The determination of the uncertainties of spectral emissivity measurements in air at the PTB. Metrologia, 2010, 47(2): S172–S181
48. Adibekyan A, Monte C, Kehrt M, Gutschwager B, Hollandt J. Emissivity measurement under vacuum from 4 μm to 100 μm and from –40°C to 450°C at PTB. International Journal of Thermophysics, 2015, 36(2–3): 283–289
49. Burleigh D D, Hanssen L M, Cramer K E, Mekhontsev S N, Khromchenko V B, Peacock G R. Infrared spectral emissivity characterization facility at NIST. In: Proceedings of SPIE—The International Society for Optical Engineering (Thermosense 26), Orlando, FL, USA, 2004, 5404: 1–12
50. Wang L P, Zhang Z M. Measurement of coherent thermal emission due to magnetic polaritons in subwavelength microstructures. Journal of Heat Transfer, 2013, 135(9): 091505
51. Yuan Z, Zhang J, Zhao J, Liang Y, Duan Y. Linearity study of a spectral emissivity measurement facility. International Journal of Thermophysics, 2009, 30(1): 227–235
52. Balat-Pichelin M, Sans J L, Escape C, Combes H. Emissivity of Elgiloy and pure niobium at high temperature for the Solar Orbiter mission. Vacuum, 2017, 142: 87–95
53. Ma J, Zhang Y, Wu L, Li H, Song L. An apparatus for spectral emissivity measurements of thermal control materials at low temperatures. Materials (Basel), 2019, 12(7): 1141
54. Honnerová P, Martan J, Kučera M, Honner M, Hameury J. New experimental device for high-temperature normal spectral emissivity measurements of coatings. Measurement Science & Technology, 2014, 25(9): 095501
55. Honner M, Honnerová P, Kučera M, Martan J. Laser scanning heating method for high-temperature spectral emissivity analyses. Applied Thermal Engineering, 2016, 94: 76–81
56. Donaldson Hanna K L, Greenhagen B T, Patterson W R III, Pieters C M, Mustard J F, Bowles N E, Paige D A, Glotch T D, Thompson C. Effects of varying environmental conditions on emissivity spectra of bulk lunar soils: application to Diviner thermal infrared observations of the Moon. Icarus, 2017, 283: 326–342
57. Cao G, Weber S J, Martin S O, Malaney T L, Slattery S R, Anderson M H, Sridharan K, Allen T R. *In situ* measurements of spectral emissivity of materials for very high temperature reactors. Nuclear Technology, 2011, 175(2): 460–467
58. Gorewoda J, Scherer V. Influence of carbonate decomposition on normal spectral radiative emittance in the context of oxyfuel combustion. Energy & Fuels, 2016, 30(11): 9752–9760
59. Gorewoda J, Scherer V. Normal radiative emittance of coal ash sulfates in the context of oxyfuel combustion. Energy & Fuels, 2017, 31(4): 4400–4406
60. Hesketh P J, Zemel J N, Gebhart B. Organ pipe radiant modes of periodic micromachined silicon surfaces. Nature, 1986, 324(6097): 549–551
61. Hesketh P, Gebhart B, Zemel J. Measurements of the spectral and directional emission from microgrooved silicon surfaces. Journal of Heat Transfer, 1988, 110(3): 680–686
62. Kusunoki F, Kohama T, Hiroshima T, Fukumoto S, Takahara J, Kobayashi T. Narrow-band thermal radiation with low directivity by resonant modes inside tungsten microcavities. Japanese Journal of Applied Physics, 2004, 43(8A): 5253–5258
63. Sai H, Yugami H, Akiyama Y, Kanamori Y, Hane K. Spectral control of thermal emission by periodic microstructured surfaces in the near-infrared region. Journal of the Optical Society of America. A, Optics, Image Science, and Vision, 2001, 18(7): 1471–1476
64. Sai H, Yugami H, Nakamura K, Nakagawa N, Ohtsubo H, Maruyama S. Selective emission of $Al_2O_3/Er_3Al_5O_{12}$ eutectic composite for thermophotovoltaic generation of electricity. Japanese Journal of Applied Physics, 2000, 39(Part 1, No. 4A): 1957–1961
65. Kirikae D, Suzuki Y, Kasagi N. A silicon microcavity selective emitter with smooth surfaces for thermophotovoltaic power generation. Journal of Micromechanics and Microengineering, 2010, 20(10): 104006
66. Hanamura K, Kameya Y. Spectral control of thermal radiation using rectangular micro-cavities on emitter-surface for thermophotovoltaic generation of electricity. Journal of Thermal Science and Technology, 2008, 3(1): 33–44
67. Markham J R, Solomon P R, Best P E. An FT-IR based instrument for measuring spectral emittance of material at high temperature. Review of Scientific Instruments, 1990, 61(12): 3700–3708
68. Ishii J, Ono A. Fourier transform spectrometer for thermal-infrared emissivity measurements near room temperatures. In: Proceedings of SPIE—The International Society for Optical Engineering (Optical Diagnostic Methods for Inorganic Materials II), San Diego, USA, 2000, 4103:126–132
69. Nakazawa K, Ohnishi A. Simultaneous measurement method of normal spectral emissivity and optical constants of solids at high

temperature in vacuum. International Journal of Thermophysics, 2010, 31(10): 2010–2018

70. Lee G W, Jeon S, Yoo N J, Park C W, Park S N, Kwon S Y, Lee S H. Normal and directional spectral emittance measurement of semi-transparent materials using two-substrate method: alumina. International Journal of Thermophysics, 2011, 32(6): 1234–1246
71. Hatzl S, Kirschner M, Lippig V, Sander T, Mundt C, Pfitzner M. Direct measurements of infrared normal spectral emissivity of solid materials for high-temperature applications. International Journal of Thermophysics, 2013, 34(11): 2089–2101
72. Bauer W, Moldenhauer A, Oertel H. Thermal radiation properties of different metals. In: Proceedings of SPIE—The International Society for Optical Engineering (Thermosense 28), Kissimmee, FL, USA, 2006, 6205: 62050E
73. Fu T, Duan M, Tang J, Shi C. Measurements of the directional spectral emissivity based on a radiation heating source with alternating spectral distributions. International Journal of Heat and Mass Transfer, 2015, 90: 1207–1213
74. Hernandez D, Antoine D, Olalde G, Gineste J M. Optical fiber reflectometer coupled with a solar concentrator to determine solar reflectivity and absorptivity at high temperature. Journal of Solar Energy Engineering, 1999, 121(1): 31–35
75. Boubault A, Claudet B, Faugeroux O, Olalde G. Accelerated aging of a solar absorber material subjected to highly concentrated solar flux. Energy Procedia, 2014, 49: 1673–1681
76. Soum-Glaude A, Le Gal A, Bichotte M, Escape C, Dubost L. Optical characterization of $TiAlN_x/TiAlN_y/Al_2O_3$ tandem solar selective absorber coatings. Solar Energy Materials and Solar Cells, 2017, 170: 254–262
77. Wang H, Prasad Sivan V, Mitchell A, Rosengarten G, Phelan P, Wang L. Highly efficient selective metamaterial absorber for high-temperature solar thermal energy harvesting. Solar Energy Materials and Solar Cells, 2015, 137: 235–242
78. Yang Y, Taylor S, Alshehri H, Wang L. Wavelength-selective and diffuse infrared thermal emission mediated by magnetic polaritons from silicon carbide metasurfaces. Applied Physics Letters, 2017, 111(5): 051904
79. Li X F, Chen Y R, Miao J, Zhou P, Zheng Y X, Chen L Y, Lee Y P. High solar absorption of a multilayered thin film structure. Optics Express, 2007, 15(4): 1907–1912
80. Greffet J J, Carminati R, Joulain K, Mulet J P, Mainguy S, Chen Y. Coherent emission of light by thermal sources. Nature, 2002, 416 (6876): 61–64
81. Sai H, Kanamori Y, Yugami H. Tuning of the thermal radiation spectrum in the near-infrared region by metallic surface microstructures. Journal of Micromechanics and Microengineering, 2005, 15(9): S243–S249
82. Wang L P, Zhang Z M. Wavelength-selective and diffuse emitter enhanced by magnetic polaritons for thermophotovoltaics. Applied Physics Letters, 2012, 100(6): 063902
83. Zhao B, Zhang Z M. Study of magnetic polaritons in deep gratings for thermal emission control. Journal of Quantitative Spectroscopy & Radiative Transfer, 2014, 135: 81–89
84. Lee B J, Wang L P, Zhang Z M. Coherent thermal emission by excitation of magnetic polaritons between periodic strips and a metallic film. Optics Express, 2008, 16(15): 11328–11336
85. Sakurai A, Zhao B, Zhang Z M. Prediction of the resonance condition of metamaterial emitters and absorbers using LC circuit model. In: Proceedings of the 15th International Heat Transfer Conference IHTC15–9012, Begel House Inc., 2014
86. Zhao B, Wang L P, Shuai Y, Zhang Z M. Thermophotovoltaic emitters based on a two-dimensional grating/thin-film nanostructure. International Journal of Heat and Mass Transfer, 2013, 67: 637–645
87. Yeng Y X, Ghebrebrhan M, Bermel P, Chan W R, Joannopoulos J D, Soljacic M, Celanovic I. Enabling high-temperature nanophotonics for energy applications. Proceedings of the National Academy of Sciences of the United States of America, 2012, 109(7): 2280–2285
88. Rinnerbauer V, Yeng Y X, Senkevich J J, Joannopoulos J D, Soljačić M, Celanovic I. Large area selective emitters/absorbers based on 2D tantalum photonic crystals for high-temperature energy applications. In: Proceedings of SPIE—The International Society for Optical Engineering (Photonic and Phononic Properties of Engineered Nanostructures III), San Francisco, CA, USA, 2013, 8632: 863207
89. Lee B J, Fu C J, Zhang Z M. Coherent thermal emission from one-dimensional photonic crystals. Applied Physics Letters, 2005, 87 (7): 071904
90. Setién-Fernández I, Echániz T, González-Fernández L, Pérez-Sáez R B, Céspedes E, Sánchez-García J A, Álvarez-Fraga L, Escobar Galindo R, Albella J M, Prieto C, Tello M J. First spectral emissivity study of a solar selective coating in the 150°C–600°C temperature range. Solar Energy Materials and Solar Cells, 2013, 117: 390–395
91. Echániz T, Setién-Fernández I, Pérez-Sáez R B, Prieto C, Galindo R E, Tello M J. Importance of the spectral emissivity measurements at working temperature to determine the efficiency of a solar selective coating. Solar Energy Materials and Solar Cells, 2015, 140: 249–252
92. Dan A, Basu B, Echániz T, González de Arrieta I, López G A, Barshilia H C. Effects of environmental and operational variability on the spectrally selective properties of $W/WAlN/WAlON/Al_2O_3$-based solar absorber coating. Solar Energy Materials and Solar Cells, 2018, 185: 342–350
93. Jyothi J, Soum-Glaude A, Nagaraja H S, Barshilia H C. Measurement of high temperature emissivity and photothermal conversion efficiency of TiAlC/TiAlCN/TiAlSiCN/TiAlSiCO/TiAlSiO spectrally selective coating. Solar Energy Materials and Solar Cells, 2017, 171: 123–130
94. Chen J, Guo J, Chen L Y. Super-wideband perfect solar light absorbers using titanium and silicon dioxide thin-film cascade optical nanocavities. Optical Materials Express, 2016, 6(12): 3804–3813
95. Li Y, Lin C, Zhou D, An Y, Li D, Chi C, Huang H, Yang S, Tso C Y, Chao C Y H, Huang B. Scalable all-ceramic nanofilms as highly efficient and thermally stable selective solar absorbers. Nano Energy, 2019, 64: 103947
96. Chang C C, Kort-Kamp W J M, Nogan J, Luk T S, Azad A K, Taylor A J, Dalvit D A R, Sykora M, Chen H T. High-temperature refractory metasurfaces for solar thermophotovoltaic energy

harvesting. Nano Letters, 2018, 18(12): 7665–7673

97. Li W, Guler U, Kinsey N, Naik G V, Boltasseva A, Guan J, Shalaev V M, Kildishev A V. Refractory plasmonics with titanium nitride: broadband metamaterial absorber. Advanced Materials, 2014, 26(47): 7959–7965
98. Huang Y, Liu L, Pu M, Li X, Ma X, Luo X. A refractory metamaterial absorber for ultra-broadband, omnidirectional and polarization-independent absorption in the UV-NIR spectrum. Nanoscale, 2018, 10(17): 8298–8303
99. Rinnerbauer V, Lenert A, Bierman D M, Yeng Y X, Chan W R, Geil R D, Senkevich J J, Joannopoulos J D, Wang E N, Soljačić M, Celanovic I. Metallic photonic crystal absorber-emitter for efficient spectral control in high-temperature solar thermophotovoltaics. Advanced Energy Materials, 2014, 4(12): 1400334
100. Li P, Liu B, Ni Y, Liew K K, Sze J, Chen S, Shen S. Large-scale nanophotonic solar selective absorbers for high-efficiency solar thermal energy conversion. Advanced Materials, 2015, 27(31): 4585–4591
101. Sai H, Yugami H, Kanamori Y, Hane K. Solar selective absorbers based on two-dimensional W surface gratings with submicron periods for high-temperature photothermal conversion. Solar Energy Materials and Solar Cells, 2003, 79(1): 35–49
102. Sakakibara R, Stelmakh V, Chan W R, Ghebrebrhan M, Joannopoulos J D, Soljačić M, Čelanović I. Practical emitters for thermophotovoltaics: a review. Journal of Photonics for Energy, 2019, 9(3): 032713
103. Datas A, Martí A. Thermophotovoltaic energy in space applications: review and future potential. Solar Energy Materials and Solar Cells, 2017, 161: 285–296
104. Tervo E J, Bagherisereshki E, Zhang Z M. Near-field radiative thermoelectric energy converters: a review. Frontiers in Energy, 2018, 12(1): 5–21
105. Heinzel A, Boerner V, Gombert A, Bläsi B, Wittwer V, Luther J. Radiation filters and emitters for the NIR based on periodically structured metal surfaces. Journal of Modern Optics, 2000, 47(13): 2399–2419
106. Marquier F, Joulain K, Mulet J P, Carminati R, Greffet J J, Chen Y. Coherent spontaneous emission of light by thermal sources. Physical Review. B, 2004, 69(15): 155412
107. Maruyama S, Kashiwa T, Yugami H, Esashi M. Thermal radiation from two-dimensionally confined modes in microcavities. Applied Physics Letters, 2001, 79(9): 1393–1395
108. Sai H, Kanamori Y, Yugami H. High-temperature resistive surface grating for spectral control of thermal radiation. Applied Physics Letters, 2003, 82(11): 1685–1687
109. Sai H, Yugami H. Thermophotovoltaic generation with selective radiators based on tungsten surface gratings. Applied Physics Letters, 2004, 85(16): 3399–3401
110. Kondo T, Hasegawa S, Yanagishita T, Kimura N, Toyonaga T, Masuda H. Control of thermal radiation in metal hole array structures formed by anisotropic anodic etching of Al. Optics Express, 2018, 26(21): 27865–27872
111. Fang J, Xuan Y, Li Q, Fan D, Huang J. Investigation on the coupling effect of thermochromism and microstructure on spectral properties of structured surfaces. Applied Surface Science, 2012, 258(18): 7140–7145
112. Huang J G, Xuan Y M, Li Q. Narrow-band thermal radiation based on microcavity resonant effect. Chinese Physics Letters, 2014, 31 (9): 094207
113. Fan D, Li Q, Xuan Y M, Xia Y. Thermal radiation from silicon microcavity coated with thermochromic film. Solar Energy Materials and Solar Cells, 2016, 144: 331–338
114. Woolf D, Hensley J, Cederberg J G, Bethke D T, Grine A D, Shaner E A. Heterogeneous metasurface for high temperature selective emission. Applied Physics Letters, 2014, 105(8): 081110
115. Stelmakh V, Rinnerbauer V, Chan W R, Senkevich J J, Joannopoulos J D, Soljacic M, Celanovic I. Performance of tantalum-tungsten alloy selective emitters in thermophotovoltaic systems. In: Proceedings of SPIE—The International Society for Optical Engineering, (Energy Harvesting and Storage: Materials, Devices, and Applications V), Baltimore, MD, USA, 2014, 9115: 911504
116. Stelmakh V, Rinnerbauer V, Chan W R, Senkevich J J, Joannopoulos J D, Soljacic M, Celanovic I. Tantalum-tungsten alloy photonic crystals for high-temperature energy conversion systems. In: Proceedings of SPIE—The International Society for Optical Engineering (Photonic Crystal Materials and Devices XI), Brussels, Belgium, 2014, 9127: 91270Q
117. Lee B J, Chen Y B, Zhang Z M. Surface waves between metallic films and truncated photonic crystals observed with reflectance spectroscopy. Optics Letters, 2008, 33(3): 204–206
118. Lee B J, Zhang Z M. Indirect measurements of coherent thermal emission from a truncated photonic crystal structure. Journal of Thermophysics and Heat Transfer, 2009, 23(1): 9–17
119. Lin S Y, Moreno J, Fleming J G. Three-dimensional photonic-crystal emitter for thermal photovoltaic power generation. Applied Physics Letters, 2003, 83(2): 380–382
120. Lee J H, Kim Y S, Constant K, Ho K M. Woodpile metallic photonic crystals fabricated by using soft lithography for tailored thermal emission. Advanced Materials, 2007, 19(6): 791–794
121. Qi M, Lidorikis E, Rakich P T, Johnson S G, Joannopoulos J D, Ippen E P, Smith H I. A three-dimensional optical photonic crystal with designed point defects. Nature, 2004, 429(6991): 538–542